Rev. Adv. Mater. Sci. 30 (2012) 1-26

ION IMPLANTATION OF POLYMERS: FORMATION OF NANOPARTICULATE MATERIALS

Vladimir N. Popok

Department of Physics and Nanotechnology, Aalborg University, 9220 Aalborg Øst, Denmark

Received: December 14, 2012

Abstract. The current paper presents a state-of-the-art review in the field of ion implantation of polymers. Numerous published studies of polymers modified by ion beams are analysed. General aspects of ion stopping, latent track formation and changes of structure and composition of organic materials are discussed. Related to that, the effects of radiothermolysis, degassing and carbonisation are considered. Specificity of depth distributions of implanted into polymers impurities is analysed and the case of high-fluence implantation is emphasised. Within rather broad topic of ion bombardment, the focus is put on the low-energy implantation of metal ions causing the nucleation and growth of nanoparticles in the shallow polymer layers. Electrical, optical and magnetic properties of metal/polymer composites are under the discussion and the approaches towards practical applications are overviewed.

1. INTRODUCTION

The discovery of synthetic routs for fabrication of polymer materials with semiconducting properties in the 70's [1] stimulated rapid development of a new branch of electronics: organic-based functional devices. On the other hand, doping of traditional semiconductor materials (Si, Ge, GaAs, etc.) via ion implantation was one of the conventional methods at that time. Thus, ion implantation was suggested as an approach to modify properties of insulating polymers, in particular, to turn them into semiconductors [2,3]. Contrarily to the implantation of conventional semiconductors aiming in doping, the idea of ion bombardment of polymers lies in a radiation-induced disruption of chemical bonds with their subsequent cross-linking and conjugation leading to the formation of carbon-rich structures and significant enhancement of conductance in the modified layer [3-8]. Depending on the polymer type and implantation regime, the conductance can rise up to 20 orders of magnitude reaching the level of poor conductors [2,4,6,9-11].

Since ion bombardment leads to significant change of the polymer structure, it alters not only electrical properties. Optical, mechanical, and tribological characteristics undergo significant evolution and they can be tuned by controlling the implantation conditions, thus, allowing to fabricate various organic-based devices. For instance, light filters, waveguides and electro-optical modulators based on the implanted polymers can be produced [12-16]. Smoothness, hardness, adhesion, wettability, wear and chemical resistance of the polymer surfaces are also altered that, in particular, makes the implantation of organic-based materials an attractive approach for the applications in biology and medicine [17-20].

However, using ion implantation, polymer properties can be changed not only due to the irradiation-related phenomena. One can embed some impurity and fabricate a composite material. Implantation of metal ions to high fluencies leads to the formation of nanoparticles (NPs). Hence, composite metal/polymer nanostructured materials can be

Corresponding author: V.N. Popok, e-mail: vp@nano.aau.dk

produced which are of great interest for a number of practical applications. In particular, shallow metal implantation of polymers is of importance for plastic electronics. By varying the metal species, ion fluence and current one can control insulator-to-metal transition (IMT) and provide evolution of mechanisms of the electrical charge transport from variable range hopping (VRH) through the carbon-rich phase of the polymer and metal inclusions up to pure electron conductance via percolating metal NPs [21-24]. Some interesting applications combining electrical and mechanical properties of metal-implanted polymers, for example, as strain gauges are suggested [25]. Optical plasmon resonance and high values of third-order optical susceptibility of the dielectrics with gold, silver and copper NPs attract a lot of research attention [26-30]. These effects are considered to be promising for nanoscale plasmonics [31] and fabrication of nonlinear optical devices [27]. Ion synthesis of transition metal NPs in various polymer substrates has been extensively studied due to the interest in superparamagnetic and ferromagnetic properties that can be utilised for developing of magnetic date storage media, magneto-sensors and magneto-optical devices [32-36].

Thus, a considerable knowledge about general aspects of ion stopping and related to it compositional and structural alterations of polymer materials is already acquired as well as a number of applied-oriented research results are published especially during the last two decades. At the current stage, it is natural to summarize these data and overview them. Since the topic of ion implantation is rather broad, the low-energy regime with typical values from a few up to ca. 100 keV is mainly considered. This energy regime is especially important for high-fluence metal ion implantation leading to nucleation of NPs in shallow polymer layers. Electronic, optical and magnetic properties of such nanocomposite materials are under the discussion.

2. COMPOSITIONAL AND STRUCTURAL ALTERATIONS

2.1. Ion stopping and latent track formation

Effect of ion implantation on structure and composition of polymers is a complex phenomenon. A number of physical and chemical processes originated by the interaction of the impacting ions with polyatomic target must be taken into account. These processes depend on the implantation energy and mechanisms of energy transfer as well as on the composition and structure of a pristine polymer. Even for low-energy regimes, the density of energy can be as high as a few hundreds eV per 1 nm of ion track length. Taking into account that the bond dissociation energy in polymers does not exceed 10 eV [9], the energy deposited by the projectile leads to multiple breakage of the chemical bonds within and around the ion path. This highly-disordered area along the ion trajectory is often called a latent track [37]. The phenomenon of radiation-induced degradation of polymer structure is often referred as radiolysis [9].

It is experimentally shown that the latent tracks are stable in most cases and they are not recovered even for long period after the implantation. This property is used for formations of filters with tiny pores (submicron diameter) by high-energy through polymer implantation with subsequent etching of the radiation-damaged track volumes, see for example [38]. After a number of experimental and theoretical investigations on the track formation, the following picture became the most commonly accepted one. Radial structure of the latent track represents a core with surrounding shell or penumbra. The cores are often experimentally identified with the cavities or craters on the polymer surface [39,40]. The core radius ranges from ca. 1 to 10 nm depending on the implantation regime, ion species and type of polymer [37,39,41-43]. The core is characterised by lower material density because of the intensive bond breakage and formation of the low-mass fragments. Some of them could be volatile and escape out from the polymer by diffusion. This phenomenon is called degassing and it will be discussed later. The surrounding penumbra presents less damaged, usually cross-linked material. With increasing distance from the track axis the concentration of the cross-links declines slowly and the composition tends to that characteristic for the pristine polymer. Density of the radiation defects also changes along the track, i.e. in longitudinal direction, depending on the implantation energy and ion mass.

The density of energy released in the track core is rather high that leads not only to pure radiation defect formation but also to heating. Part of the ion stopping power causes the vibration excitation of the polymer atoms on the time scale of 10^{-14}-10^{-12} s after the ion impact [3, 8]. Then, the excitation energy converts into thermalisation of the ion track volume resulting in abrupt local temperature increase which

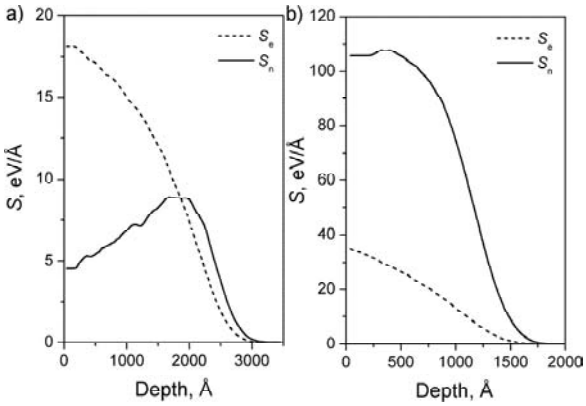

Fig. 1. Depth profiles of electronic (S_e) and nuclear (S_n) stopping powers for (a) 50 keV C^+ and (b) 150 keV Ag^+ ions in PE calculated using SRIM-2008 code.

can be described in the framework of the "thermal spike" model developed by Seitz and Koehler [44] with further refinements introduced by Sigmund [45], Kelly [46] and Bitensky with co-workers [47]. For instance, molecular dynamic simulations carried out for 240 keV C^+ ions implanted into makrofol E ($C_{16}H_{14}O_3$) show temperature of 1300K in the track core [43]. The track area gradually cools down in radial direction and the temperature decreases to 370K at 7-8 nm distance from the track axis. Thus, the thermal spike phenomenon causes the rapid local heating to temperatures much higher than the glass transition point that leads to the polymer degradation additional to that originated by the radiolysis.

While discussing the energy transfer from an ion to polymer, two principally different mechanisms should be considered: elastic nuclear collisions and inelastic electronic interactions [48]. Both mechanisms act simultaneously during the surface impact and further ion movement in the target [3]. Their contributions to the total energy loss of the projectile are characterised by nuclear and electronic stopping power, S_n and S_e, respectively. The nuclear stopping dominates for heavy ions while the electronic one – for light ions. By the term light ion in this paper, chemical elements with masses below or around 20 a.m.u. are assumed. Ratio of these stopping mechanisms in the total energy loss changes as the ion slows down. The electronic stopping dominates at the beginning of the projectile pass while the nuclear collisions prevail nearly the depth where the ions stop. Typical depth distributions of the stopping powers for light C^+ and heavy Ag^+ ions in polyethylene (PE) calculated using SRIM-2008 code [49] are presented in Fig. 1.

2.2. Degradation of polymers

Energy transfer in binary nuclear collisions leads to direct bond breakage. Since the ion energy is much higher than the binding energy of atoms in a polymer, the ion imparts enough energy to the primary replaced atom (recoil) for the following replacements thus producing non-linear collision cascades [8,48]. Energy deposition by means of the electronic stopping results in excitation of the polymer units. Taking into account the lifetime of the "electronic event" lasting up to 10^{-12} s [3], it is very probable that the excitation can migrate to a relatively long distance from the core of the track (up to 100 polymer units [6]) forming electron excitation cascades or penambra [50]. Relaxation of the excited states causes the selective scission of the weakest bonds. Hence, in contrast to inorganic materials, breakage of the chemical bonds in polymers occurs by means of both the nuclear and electronic stopping.

The bond rupture by the electron excitation is especially significant in the case of polymers with heteroatom-containing functional groups [9,11]. For instance, the implantation of polyimide (PI) with 150 keV Ne^+ or 90 keV N^+ ions (where $S_e/S_n > 6.5$) leads first to degradation of the ether linkages [51] and then to gradual converting of the imide groups into amide ones [52] with CO as a major released gaseous product [53]. Similarly, the irradiation of polyethersulfone (PES) under the conditions where the electronic stopping prevails causes selective reduction of sulfone groups to sulfoxide ones and then, under high fluences, to sulfide groups [3,54]. Example on the effect of electron excitation for the case of polyethyleneterephthalate (PET) can be found in [55]. Heterocyclic groups are more resistant to the electron excitation. However, because of the asymmetric system of delocalised π-electrons, they can also be transformed. For example, the electron beam irradiation of poly(2-vinylpyridine) results in destruction of pyridine rings and formation of amino groups [54] while the aromatic rings in PI do not degrade under the electronic stopping [3, 54]. The last fact is important in terms of further formation of polyaromatic structures with π-electrons responsible for the increase of conductance. In general, the energy transferred to the polymer host during the implantation as a result of the electronic stopping is mainly released in the reactions of dehydrogenation and weak bond breakage. These processes cause the formation of low-mass fragments and their yield has been found to be an

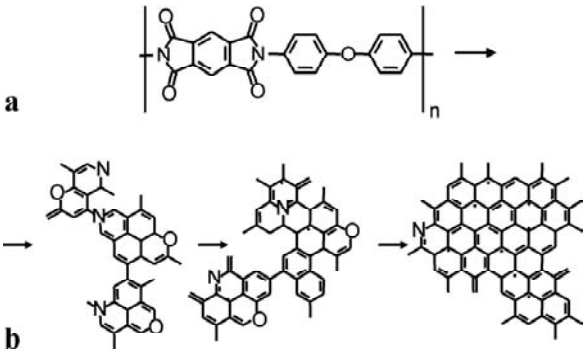

Fig. 2. (a) Chemical formula of PI elementary unit and (b) the polymer structural transformation upon implantation. According to [11].

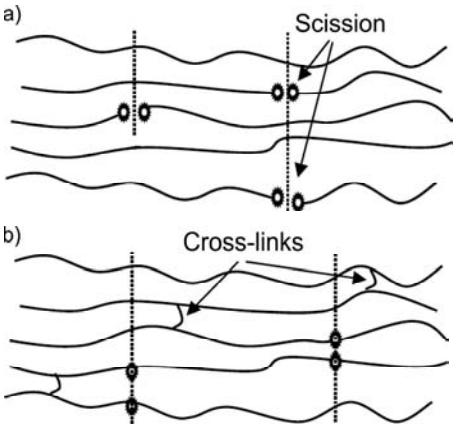

Fig. 3. Schematic representation of (a) scission of molecular polymer chains and (b) cross-linking under ion implantation.

increasing function of the electronic stopping power [56].

Increase of nuclear part in the S_e/S_n ratio fundamentally influences the character of the processes occurring in the polymer target. Massive and random rupture of the chemical bonds takes place. For instance, under the implantation of PES with 50 keV As^+ ions ($S_e/S_n < 0.2$) not only the sulfone groups are broken but acetylene splits out and gives rise to the formation of 1.4-substituted butadiene [57]. Ion implantation of PI at low S_e/S_n ratio results in both the disruption of phenyl rings and degradation of imide groups yielding a number of products: iminic and pyridinic-like groups as well as tertiary amines [3,58]. The scheme of the PI transformation under high-fluence 40 keV Ar^+ ion implantation, proposed in [11], causing the formation of extended polycondensed structures is presented in Fig. 2.

Thus, both nuclear and electronic stopping of ions in polymers lead to degradation of the organic host. There are two possible competing processes: (i) scission of molecular polymer chains resulting in fractionating and (ii) free radicals formation (branching) leading to cross-linking and bonds conjugation (Fig. 3) [5]. Efficiency of the scission or cross-linking is closely connected to the type of polymer. For example, the chain fraction formation is the most typical for polyisobutylene, whereas PE and polystyrene (PS) are mainly characterised by the cross-linking [59,60]. When the number of cross-links attains a certain critical value, the gel fractions with a three-dimensional network of bonds between macromolecules may form [60].

Since material is modified in a small volume around the individual latent track, a number of projectiles bombarding the surface or, in other words, ion fluence is crucial parameter for polymer degradation. By considering a track radius it is easy to calculate threshold fluence, at which the sample surface will be completely filled with ion tracks. At such fluence separated damaged volumes overlap and further implantation is carried out into already modified material. Therefore, one can distinguish two implantation regimes: (i) a single-track regime where the tracks are isolated from each other and (ii) a track overlapping regime. According to the above-mentioned data on the ion track parameters and results presented in [3,61,62], the transition from the single track regime to the overlapping one occurs for fluence range of 5×10^{12}-5×10^{13} cm^{-2} in the case of light ions and for lower fluences in the case of heavy ions because they produce larger in diameter latent tracks.

Radiative and thermal processes interplay in a complex manner in every latent track and, thus, represent a unified phenomenon of radiothermolysis. Products of the radiation damage are involved in the following thermalisation, which is very similar to conventional pyrolysis of polymers. For majority of polymers this process is completed at temperatures of about 1100K. Strong analogy of the polymer degradation under implantation to the pyrolysis is shown for various polymers, for instance, by studying the volatile products using infrared and mass spectroscopy [63]. In the case of implanted polymers, the high temperature in the track favour the cyclisation of the radiation-induced unsaturated chain fragments by the intramolecular Diels-Alder mechanism according to which aromatic hydrocarbons are more stable compared to linear ones at temperatures above 1100K [9]. As the track

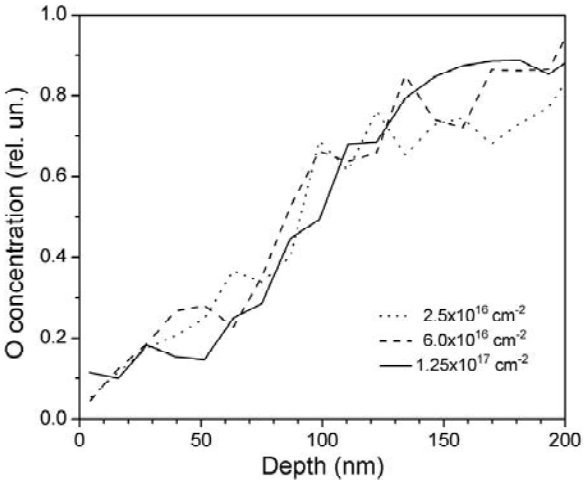

Fig. 4. Depth distribution of oxygen in PI implanted by 40 keV Fe^+ ions with various fluencies. According to [68].

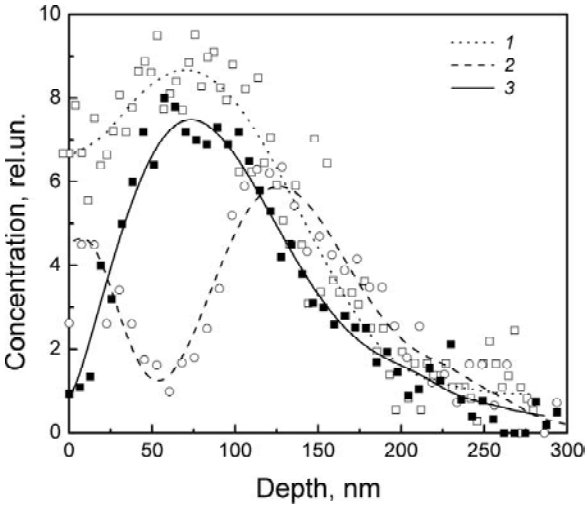

Fig. 5. Depth distribution of oxygen in PE implanted by 100 keV Sb^+ ions with fluencies of (1) $1x10^{14}$ and (2) $5x10^{15}$ cm^{-2}. Depth profile of "carbon excess" for the highest fluence is presented as graph (3). According to [72].

cooled down, the aromatic fragments are tended to be linked together and stabilised due to extension of the conjugated system [6,64].

Gaseous compounds realised in radiothermolysis processes can be emitted, thus, leading to degassing from the polymer. This phenomenon is especially pronounced for the case of low-energy implantation where the damage is formed in a shallow layer and gases can easily escape from low depth. Residual gas analysis during ion implantation reveals the yield of H_2, CH_4, C_2H_2, C_3H_5, etc. from PE and PS bombarded by 100 keV He^+ and 200 keV Ar^+ ions [2]. Large amount of saturated hydrocarbons (methane, ethane) is produced by the ion irradiation of polypropylene (PP) and polybutylene [65]. Typical molecules and fragments emitted by implanted PI are H_2, C_2H_2, CO, and CO_2 [42]. Therewith, the escape of H_2 results in dehydrogenation, CO – in amidisation etc. depending on the type of polymer. Elastic recoil detection analysis can be used for direct observation of the hydrogen depletion in polymers as was demonstrated, for instance, for PI, PET, and polyetheretherketone (PEEK) implanted by 40 keV Ni^+ ions to high fluencies [66]. Significant reduction of the hydrogen content was also observed in the nitrogen-implanted CR-39 polymer using Raman spectroscopy [67]. Change of oxygen contents can be examined by Rutherford back-scattering (RBS). An example of the near-surface depletion of oxygen in PI implanted by 40 keV Fe^+ ions is presented in Fig. 4 [68].

One of the direct consequences of the degassing is an increase of carbon ratio in the implanted layer, i.e. carbonisation of polymer [7, 69]. The enrichment of carbon can be observed, for instance, in RBS spectra. For the implanted samples, there is a bump on the background of the signal corresponding to the carbon content characterising the pristine sample. Depth profile of an "excess" in carbon concentration in polymers can be reconstructed from such spectra. The carbon "excess" is especially well pronounced in the case of implantation of heavy ions and located at a certain depth under the surface depending on the implantation energy and type of polymer [70-72]. An example of the carbon "excess" profile for the case of 100 keV Sb^+ ion implantation into PE is shown in Fig. 5, curve 3.

Depth profiles of the radiation damage can also be obtained indirectly by so-called decoration method. If the polymer does not originally contain oxygen, the post-implantation oxidation of the damaged layer can be observed under the exposure of the polymer to ambient atmosphere. Oxygen diffuses into polymer and becomes trapped on the radiation defects. It can also create relatively stable products and compounds, for instance, carbonyl and hydroxyl groups [73-75]. This effect was observed, for instance, for PE and PP implanted by various ions [70-72,76-78]. One of such profiles can be seen in Fig. 5, curve 1. However, if the polymer is implanted with high fluence leading to significant carbonisation yielding structures with conjugated bonds and minority of radicals, oxygen has lower probability to be trapped in this layer. Hence, one can find a minimum in the depth distribution of oxy-

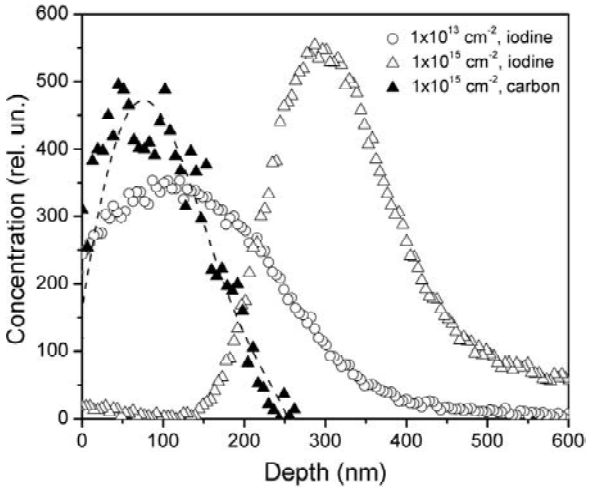

Fig. 6. Depth profiles of diffused iodine and "carbon excess" in PE implanted by 150 As^+ ions. According to [80].

gen well corresponding to the maximum of "carbon excess" as one can see comparing curves 2 and 3 in Fig. 5. Good examples of decoration of the radiation damage are also given by post-implantation diffusion of molecular iodine [79-81]. Fig. 6 shows how the iodine depth distribution evolves depending on the implantation fluence. For lower fluencies, the distribution more or less follows the profile of radiation damage introduced by ions due to the nuclear stopping. However, with fluence increase (1×10^{15} cm^{-2}) strong carbonisation of the implanted layer occurs that leads to the iodine depletion in the layer enriched by carbon [80]. Formation of similar anomalous depth profiles was also found for the Li diffusion from water solution of LiCl into the PET implanted by 150 keV Ar^+ ions [82].

Ion bombardment does not result in the complete carbonisation of the implanted layer. The effect is very sensitive to ratio between S_n and S_e because nuclear stopping is more efficient in bond rupture and, thus, in degassing. For instance, under the implantation of PE by F^+ ions, carbon concentration in the implanted layer comes to saturation at level of ca. 40 at.% [52] compared to 33 at.% in the pristine polymer. However, the carbon content reaches 65-85 at.% (depending on ion fluence) in the PE implanted by heavy As^+ ions [70,71,83]. Carbonisation process is also dependent on type of polymer and its structure. When the initial content of carbon is higher, as in the case of PI (78 at.%) and polyamide-6 (PA) (77.5 at.%), the carbon concentration in the shallow surface layer can reach 87-89 at. % under high-fluences (5×10^{16}-1×10^{17} cm^{-2}) as was, for instance, found for 100 keV B^+ ion implantation [84]. The process of the ion-induced carbonisation of polymers under implantation of heavy ions is practically accomplished at the fluence level of (1-5)$\times10^{15}$ cm^{-2}. In the case of lighter ions, this occurs at higher fluencies [19,76,77,85].

The effect of carbonisation is of considerable interest because of significant change of the structure and properties of polymers. At low implantation fluencies corresponding to single track regime, the carbon-enriched zones are formed in the latent tracks. They are often called pyrocarbon "droplets" or clusters [76,85]. This structural rearrangement occurs through the condensation of the aromatic and unsaturated fragments and results in sp^2 bonded carbon atoms. Formation of the carbon clusters is found using transmission electron microscopy (TEM) and neutron scattering measurements. Sizes of the inclusions vary from a few to a few tens of nm [86,87]. Optical spectroscopy study reveals nucleation of carbon clusters of about 2 nm in size in PE and PA implanted by 100 keV boron and nitrogen ions [85,88]. For the case of high-fluence Ar^+ ion implantation in CR-39 polymer with energy of 130 keV, the number of carbon atoms per cluster was found to reach a couple of hundreds [89] that is consistent with the above-mentioned microscopy measurements. With fluence increase, the latent tracks overlap and the π-bonded carbon clusters grow and aggregate forming the network of conjugated C=C bonds. At very higher fluencies it leads to the growth of a quasi-continuous carbonaceous layer buried under the polymer surface [90] which can even be transformed into the phase mostly consisting of amorphous carbon or graph-

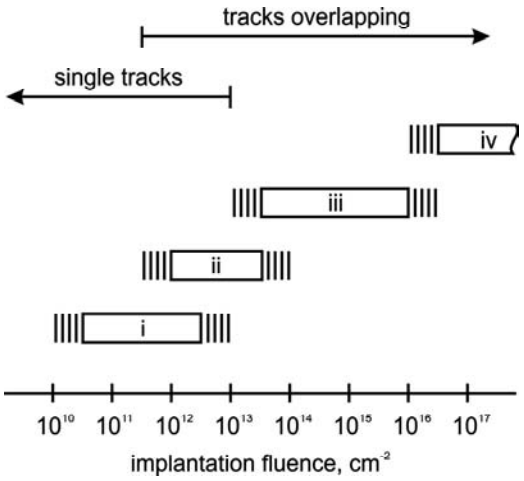

Fig. 7. Stages of polymer carbonisation versus implantation fluence. See text for details.

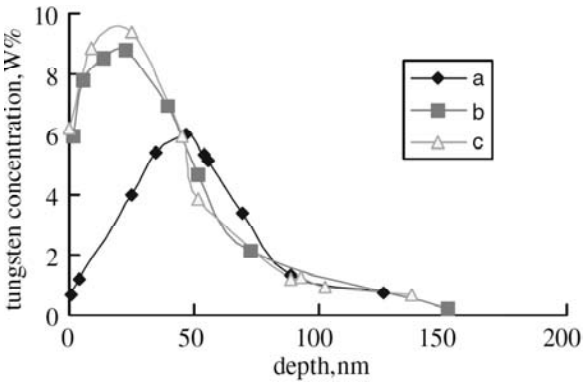

Fig. 8. Depth profiles of 40 keV tungsten implanted into PET with fluencies of (a) $5x10^{16}$, (b) $1x10^{17}$ and (c) $2x10^{17}$ cm^{-2}. Reprinted from [96] with permission from Elsevier.

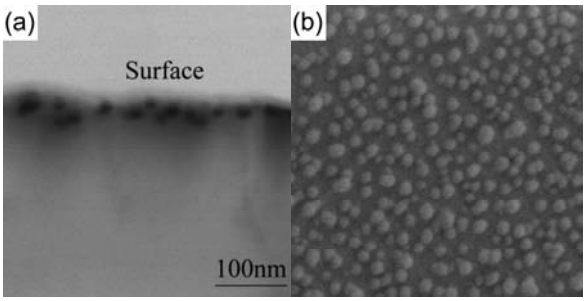

Fig. 9. (a) Scanning TEM image (in cross-section) and (b) SEM image (frame size is 600x600 nm) of PET implanted by 40 keV tungsten ions with fluence of $1x10^{17}$ cm^{-2}. Reprinted from [96] with permission from Elsevier.

ite-like material [91]. For some cases of the high-fluence implantation of gas and carbon ions in polymer films, the formation of diamond like carbon inclusions with sp^3 bonds was found using Raman spectroscopy [92].

Following stages of carbonaceous phase formation with increase of ion fluence were suggested for polymers in [69]: (i) degassing, transformation of functional groups and cross-linking within the latent track areas of the polymer resulting in formation of "pre-carbon" structures; (ii) nucleation and growth of the carbon-enriched clusters; (iii) aggregation of the carbon clusters up to formation of the quasi-continuous carbonaceous buried layer characterised by the network of conjugated bonds; (iv) transition of the carbonised phase to amorphous carbon or graphite-like material. The corresponding diagram is presented in Fig. 7. It is also obvious that both the degassing and carbonisation phenomena lead to compaction of the implanted layer: polymer density can increase factor of 2 for high fluencies [92].

3. DEPTH DISTRIBUTION OF IMPLANTED IMPURITIES

3.1. Projected ranges and diffusion

An incident ion slows down in a matter due to the interactions with nuclei and electrons and finally comes to rest at some depth called projected range R_p (projection of the total pathlength on the direction of penetration). Stopping of ions and their R_p can be modelled, for instance, using Monte-Carlo method. In particular, one of the well-known simulation codes SRIM is found to be rather well predicting depth profiles of various ions for the wide spectrum of solid state materials [49]. However, for polymers, the experimentally obtained depth distributions of the implanted species in many cases differ significantly from the simulated ones. As the typical implantation fluencies required for many applications are between 1×10^{14} - 1×10^{16} cm^{-2}, this leads to significant alteration of structure and composition of polymers. In particular, the carbonisation causes compaction, thus, the increase of density. It is worth noting that this is a continuous process, i.e. the polymer undergo a gradual change in structure and composition during the implantation. Hence, the final depth profile can be represented as a sum of the depth distributions accumulated during various stages of the implantation. As a result, R_p is found to be 10-30% shorter (especially for heavy ions) and a range straggling ΔR_p can be up to 120% higher in the experiments compared to the simulations by SRIM [93-95]. In Fig. 8 the experimental depth profiles of W implanted in PET are presented [96]. One can clearly see that with the fluence increase the profile shapes convert from the Gaussian-like to asymmetric ones and the maximum of concentration shifts towards surface due to the effects of ion mixing, target compaction and surface sputtering. At very high fluencies the implanted tungsten atoms form NPs in the ultra-shallow layer (Fig. 9a). These particles are partly towered above the surface as one can see in scanning electron microscopy (SEM) image shown in Fig. 9b. Computer codes including change of the near-surface layer composition due to cascade atom mixing as well as sputtering of the surface layer lead to more precise predictions of depth distribution of the implanted species. Examples of such codes are TRYDIN and

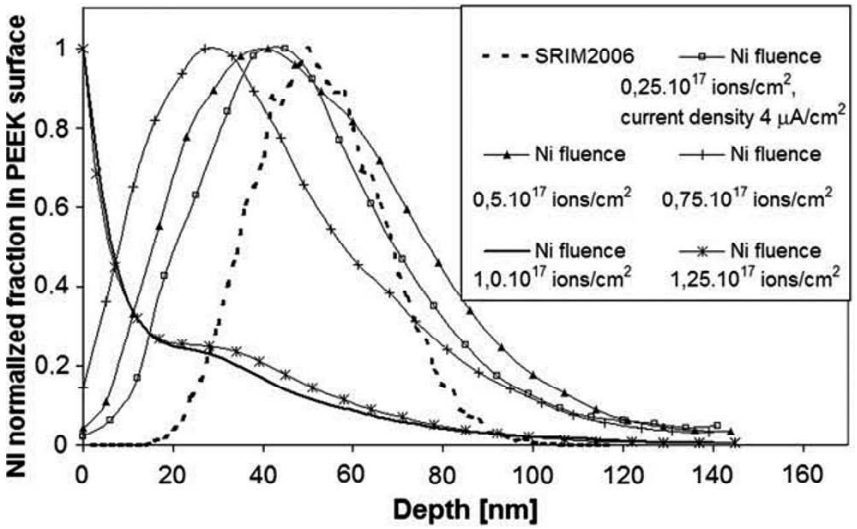

Fig. 10. Depth profiles of Ni implanted with energy of 40 keV and various fluencies into PEEK. The profile calculated using SRIM-2006 is presented as dashed line. Reprinted from [66] with permission from Elsevier.

DYNA [97,98]. For instance, in the case of 60 keV implantation of silver and copper ions into PMMA, it was shown that TRYDIN quite well predicts depth distribution of the metals demonstrating shift of the concentration maximum towards surface with fluence increase [99]. Similar tendency was recently reported for 60 keV Ni^+ ions implanted into polycarbonate (PC), PI, PET and PEEK [25,66]. However, in the case of extremely high fluencies (over 1×10^{17} cm^{-2}) anomalous depth profiles were found (Fig. 10). They are characterised by the decrease of Ni concentration and surface-located maximum of the depth distribution. Atomic force microscopy (AFM) images show very high surface erosion [100] which could be caused not only by the very high fluencies but also by relatively high ion current densities (4-10 μA/cm^2) leading to significant heating of the surface and possible thermal degradation.

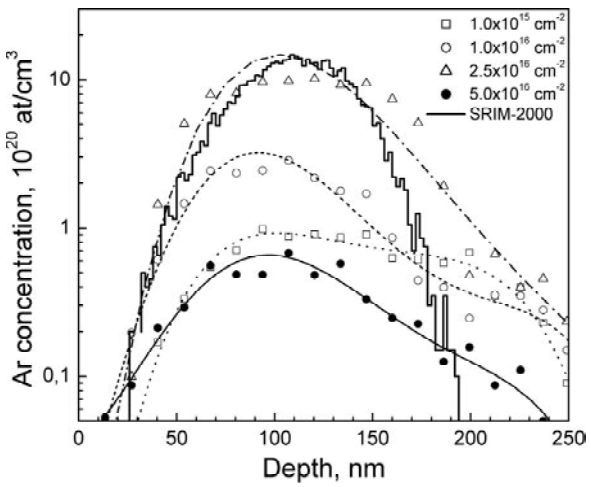

Fig. 11. Depth profiles of 80 keV argon implanted into PI with various fluencies. The profile calculated using SRIM-2000 code is presented as well (in rel. un.). According to [11].

One more important phenomenon which changes final depth distribution of the implanted impurity is diffusion. For instance, experimental R_p values were observed to be more than 2 times higher compared to the simulated ones for inert gases (Ar, Xe, and Kr) [93,101]. These profiles typically demonstrate long inward tails. The experimentally obtained values of the diffusion coefficient follow Arrhenius type of behaviour.

In the case of very high-fluence (> 1×10^{17} cm^{-2}) and low energy (50 keV) Xe^+ ion implantation, where the projected range in the polymer is rather short, the layer concentration of the implanted xenon was found to be much lover than the fluence value [102]. It was suggested that some part of the implanted gas atoms undergoes diffusion towards the surface and escapes from the polymer. Similar effect was observed for PI implanted by 80 keV Ar^+ ions to very high fluences (Fig. 11) [11]. Furthermore, Ar atoms implanted with 40 keV to high fluencies were not found in the polymer at all [11]. In this case, the diffusion-stimulated escape of the gas atoms was intensified by heavy sputtering of the polymer. AFM images demonstrate the surface disorder with roughness of about 30 nm (Fig. 12) which is comparable with R_p for this implantation. The same phenomenon of absence of Ar was reported for the polytetrafluoroethylene (PTFE) implanted with en-

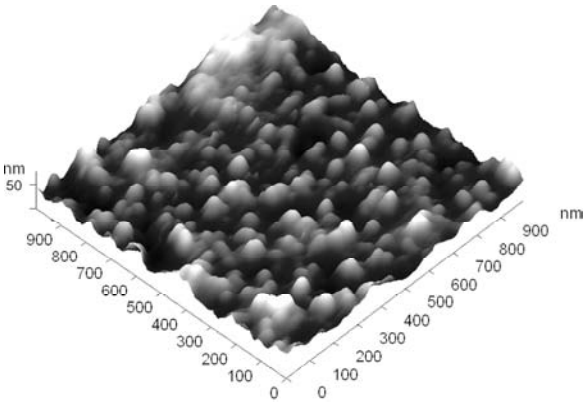

Fig. 12. AFM image of PI surface implanted by 40 keV Ar^+ ions with fluence of 7.5×10^{16} cm^{-2} at ion current density of 8 $\mu A/cm^2$.

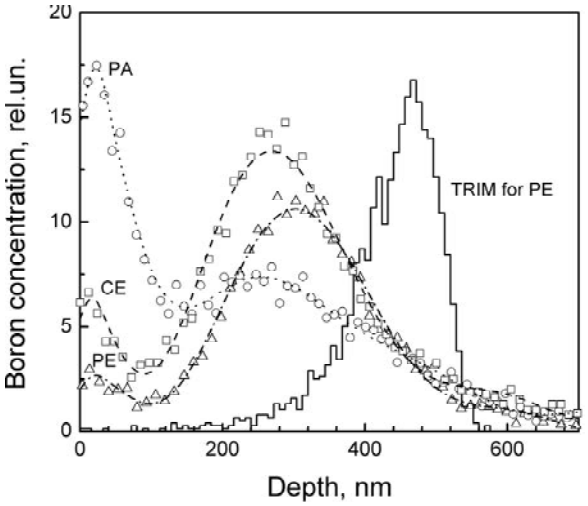

Fig. 13. Depth distributions of boron implanted with energy of 100 keV and fluence of 5×10^{16} cm^{-2} into PA, PE and cellulose (CE). The profile calculated using TRIM-95 code is presented as well. According to [85].

ergy of 30 keV and fluencies of 1×10^{15} and 1×10^{16} cm^{-2} [103].

Diffusion has an especially significant effect on the distribution of light species implanted into polymers. For instance, early experiments on $^6Li^+$ and $^{10}B^+$ ion implantation show that the resulting depth profiles are close in shape to those predicted for the electronic stopping of the ions [104]. The impurities diffuse towards the surface and they are captured by the radiation defects produced due to the ionisation effects dominating in the total stopping energy loss. It is shown that the transition from the regular depth distribution to the "ionised" one takes place if the contribution of the electronic stopping is significantly high compared to the nuclear stopping ($S_e \approx$ (2-5) S_n) [105]. Later models show that the implanted atoms are redistributed immediately after their ballistic slowing-down. The mobility of the implant is enhanced in the radiation-damaged layer and the local diffusion enhancement as well as trapping being controlled by the electronic stopping [106]. It is also found that the shape of the depth profiles changes with increase of both the fluence and implantation energy [106,107]. By the example of boron implantation into various polymers, it is observed that the profiles become bimodal at high fluences [85,108]. The boron distribution consists of a bulk maximum and a surface peak (Fig. 13). The bulk part of the profile resembles more or less the distribution of collision energy transfer (due to the nuclear stopping). The surface peak appears as a result of the diffusion presumably via the latent tracks.

Another case of diffusion-induced distribution was found for the polymers implanted with high fluences (10^{16}-10^{17} cm^{-2}) of 40 keV cobalt and iron ions [68,109]. Beyond the near-surface peak, the depth distributions exhibit inward tails with weakly-pronounced additional maxima of concentration of Fe and Co atoms (Fig. 14). The inward tail is most probably related to both an appearance of strain waves and a heating of polymer surface under the implantation with rather high ion current densities (4-12 $\mu A/cm^2$) stimulating rapid metal diffusion into the polymer bulk. The strains could appear as a result of "free volumes" formed due to the degassing of the volatile compounds and compacting of the surface layer due to the carbonisation. One can also not exclude the formation of cracks to the depth

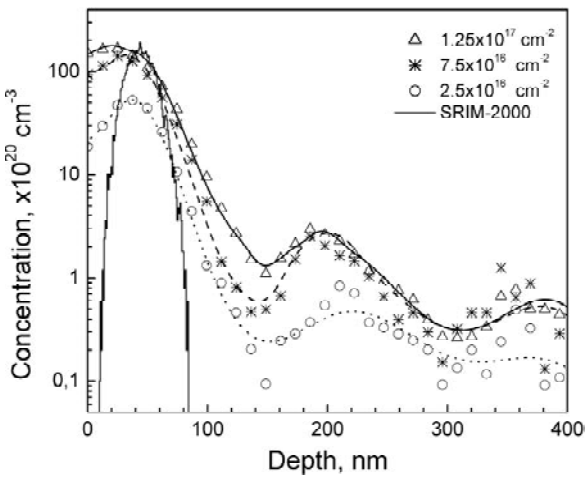

Fig. 14. Depth profiles of cobalt implanted with energy of 40 keV and various fluencies into PI. The profile calculated using SRIM-2000 code is presented as well (in rel. un.). According to [109].

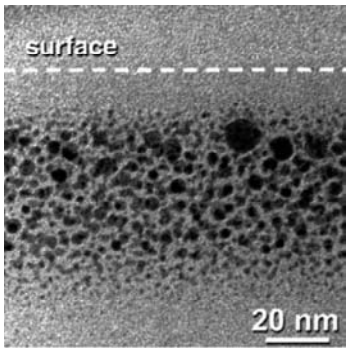

Fig. 15. TEM cross-sectional image of NPs nucleated in PI implanted by 100 keV Au^+ ions with fluence of $5x10^{16}$ cm^{-2}. Reprinted with permission from [121]. © 2004, The American Physical Society.

exceeding the implanted region due to the above-mentioned reasons. Similar surface damages were observed, for example, on polyetherimide and PTFE implanted to high fluences [110, 111]. Nucleation of metal NPs under high-fluence implantation (above ca. 1×10^{16} cm^{-2}) should be also taken into account while considering alteration of polymer structure and composition. This topic is discussed below.

3.2. Nucleation of metal NPs

Polymer composites containing metal NPs can be prepared using several ways: by chemical synthesis in an organic solvent [29], vacuum deposition on viscous polymers [112], plasma polymerisation combined with metal evaporation [113] etc. All these methods have advantages and disadvantages. Some of common problems are: a low filling factor and a large dispersion in sizes and shapes of NPs. Ion implantation enables a high metal filling factor to be reached in a solid matrix beyond the equilibrium limit of solubility. The system relaxes by precipitation of metal as the NPs. Advantage of the method is in a possibility to form any composite of metal/dielectric [3,6,69]. One can also control depth at which NPs are formed and to a certain extent size of NPs. First studies on ion synthesis of metal NPs in dielectrics are dated by the beginning of the 70's. Particles of Na, K, and Au were formed in non-organic glasses and crystals [114,115]. The formation of particles in organic matrices was realised at the beginning of the 80's by Koon and co-workers [116,117] in their experiments on implantation of Fe ions into polymers.

Threshold fluences at which the particles start nucleating are found to be about 1×10^{16} cm^{-2} for majority of polymers. NPs can be directly observed using TEM [100,110,118-120]. One of the examples is shown in Fig. 15 [121]. Metal clustering in polymers is caused by the high metal cohesive energy and low metal-polymer interaction energy. Process of nucleation of NPs in the implanted layer consists of a few stages: metal accumulation up to supersaturation, formation of few-atoms nuclei and their growth [28]. Assuming that the NP growth occurs by successive joining of the single atoms one can conclude that the process is governed by both the local concentration of metal and diffusion coefficient. The particles nucleated at fluencies just slightly above the threshold one are usually spherical in shape. Mean size (diameter) depends on type of both the metal and polymer. For instance, for Ag and Cu the size is found to be about few nm in epoxy resin [119] and PMMA [120]. About same sizes were determined for Au NPs in PI and polydimethylsiloxane (PDMS) [121,122] and for Ni NPs in PI and PET [100]. While for high-fluence Fe implantation in PMMA and PI, the particle size could reach a couple tens of nm [32,120,123]. It is also experimentally found that NPs of the same metal has tendency to reduce in size with increase of specific density of the polymer substrate [35].

One of disadvantages of ion implantation is statistically non-uniform distribution of the metal atoms over the depth. This leads to a size dispersion of NPs. Larger in size particles are formed at the depth corresponding to highest concentration, i.e. to R_p of the metal ions. Increase of ion fluence typically leads to enlargement of the NPs followed by widening of the size distribution. Growth of the metal NPs is affected by many factors: metal concentration, mobility of atoms and parameters of the polymer media such as composition and structure which undergo drastic alteration under the high-fluence implantation. Carbonisation and radiation-induced disordering of the structure effect the metal diffusion. Polymer viscosity is found to be playing important role for the NP nucleation and growth [124]. Ostwald ripening, where smallest particles dissociate and released metal atoms enlarge other NPs, is one of the mechanisms playing important role in the growth process, especially at high ion current density implantation regimes.

As briefly mentioned in section 3.1, one of the consequences of high-fluence ion implantation is sputtering of polymer target. Sputtering rates of polymer materials are few times higher compared to metal atoms incorporated into substrate during the implantation. For low-energy implantation, metal NPs are formed just beneath the surface and, thus, sputtering of thin polymer layer at later stage of

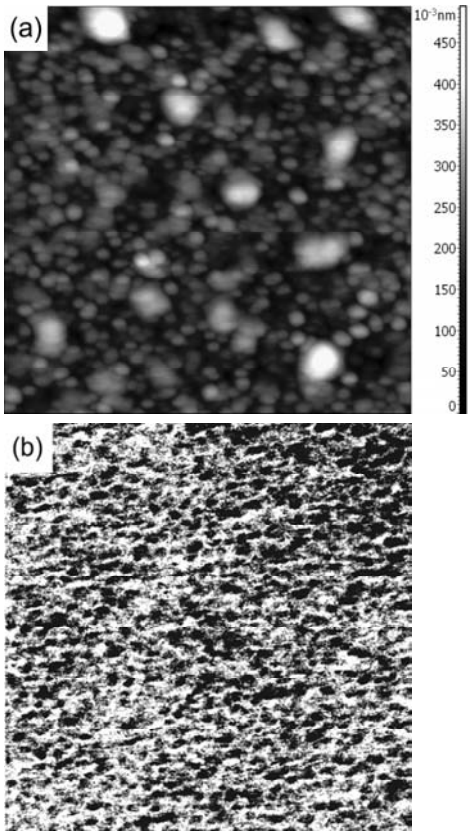

Fig. 16. (a) AFM and (b) SEM images of PI surface implanted by 40 keV Cu^+ ions with fluence of $1.25x10^{17}$ cm^{-2} at ion current density of 12 μA/cm^2. Size of the frames in both panels is 2x2 μm. Both images reveal the metal NPs just below and at the surface level.

implantation leads to the towering of already nucleated (at earlier stage of implantation) very shallow-located NPs. AFM is one of the methods that can image these towered NPs as hemispherical protrusions. Such a possibility was demonstrated for shallow-implanted crystalline dielectrics [125-127] as well as for polymers [68,100,128,129]. Using both topography and phase imaging it was possible to prove that the observed surface protrusions correspond to metal NPs [130]. Good correlation between the images obtained using AFM and TEM [128] as well as AFM and SEM was obtained. See, for instance, Fig. 16 showing the AFM and SEM images of the same sample of PI with the NPs formed in the result of high-fluenece copper implantation.

At very high fluencies, the nucleated NPs start agglomerating that can result in formation of worm-like structures as shown for the case of Fe in PET in Fig. 17. Very similar surface topography was observed by AFM for the high-fluence implantation of Au into PDMS [131]. However, not all implanted atoms contribute to the formation of metal NPs. In the case of Fe and Co, it is measured that NPs contain only up to 65% of atoms implanted into PI with fluence of 1.25×10^{17} cm^{-2} [35,123]. The rest is still in atomic form. Phase analysis of the metal/polymer composites synthesised by the implantation shows that: iron preferably forms NPs of α-Fe with some contribution of Fe_3O_4 phase in various polymers [35,120]; cobalt NPs in PI are pure metallic with small fraction bounded to carbonyl group [68] (this fraction is most probably formed by atomic Co, not by Co of the NPs); Ag NPs in PMMA have fcc structure, no chemical compounds with silver atoms are found [28]; Cu NPs in PMMA are formed from both the pure metallic phase and Cu_2O [120].

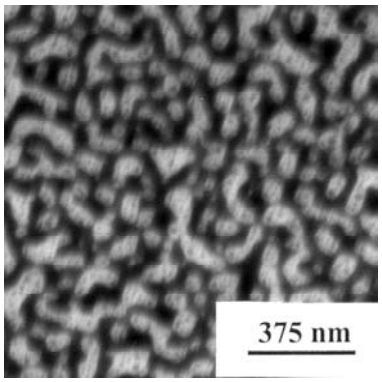

Fig. 17. TEM in plane image of PET implanted by 40 keV Fe^+ ions with fluence of $1.5x10^{17}$ cm^{-2}. According to [128].

It is worth mentioning one more interesting approach to synthesize metal NPs based on irradiation of viscous polymers [124,132,133]. The use of the viscous state of the polymer offers a possibility to increase the diffusion coefficient of the implanted impurities up to 8-10 orders of magnitude at room temperature [132]. Thus, the growth of metal NPs is consistent with homogeneous diffusion mechanism in contrast to heterogeneous mechanism in solid state polymers. After the implantation, the viscous matrix can be transformed into the solid-state. Ion synthesis of Co NPs in viscous epoxy has shown that the size and crystalline structure of the particles can be tuned by change of the polymer viscosity [133].

4. PROPERTIES OF IMPLATED POLYMERS

4.1. Electrical properties

Implantation-induced disorder of polymers leads to alteration of electronic structure and, thus, to change

of conductance. Typically, conductance increases with ion fluence due to the carbonisation of the polymer. An exception is the high-fluence implantation of metals where the formation of NPs and increase of metal volume fraction also contribute to the charge carrier transport. This phenomenon will be discussed separately below.

In arbitrary case, the conductance only slightly depends on the ion species being mainly determined by the energy transfer to polymer matrix during the stopping of ions [2,134,135]. Depending on type of polymer and implantation parameters (fluence, energy, ion current density and temperature) it is possible to vary the resistivity within ca. 20 orders of magnitude starting from pure dielectrics (ca. 10^{15}-10^{18} Ω·cm) and ending in the range of poor conductors (10^{-1}-10^{-3} Ω·cm). An example, how the resistance decreases with the increase of ion fluence, is shown in Fig. 18 for the case of Ar-implanted PI. The graphs also demonstrate good correlation of conductance and optical band gap. This topic will be discussed in more detail in section 4.2. It is worth noting that for the same implantation conditions the conductance can differ for a few orders of magnitude for diverse polymers due to the difference in the structural and compositional alterations under the ion-beam treatment.

Due to the carbonisation the carbon atoms have tendency to clusterisation with sp^2 hybridisation. This type of chemical bonding possesses unpaired π-electrons which become charge carriers in the implanted polymers [136]. The most probable mechanisms providing the charge carriers transport between the clusters is hopping or tunnelling [102]. Since the conducting phase in the implanted layer is formed of the discrete clusters the conductance has a threshold character showing the percolation transition for the fluence range corresponding to the track overlapping. This percolation behaviour is confirmed by number of publication [2,135,137] and discussed in detail, for instance, in [6,9]. A stick-slip nature in the conductivity dependence with subsequent saturation (plateau effect), which can be seen in Fig. 18 and found for various polymers implanted to high fluences [11,138-141], is in good agreement with the structural alteration of polymers towards materials containing amorphous carbon or graphite-like structures as described in section 2.2.

Measurements of temperature dependence of conductance or resistance give more detailed information on the mechanisms of charge transport. In general, the temperature dependence of conductivity σ can be described in terms of following equation

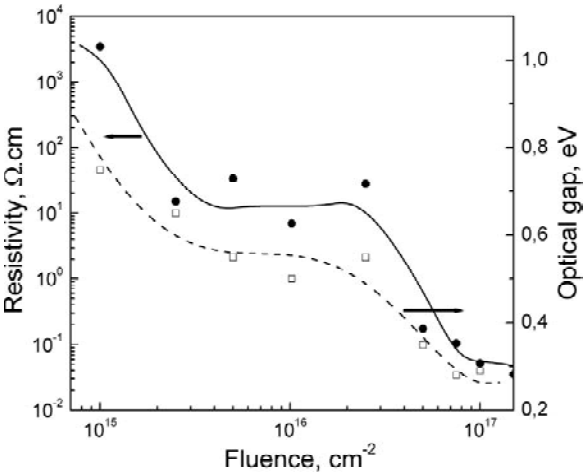

Fig. 18. Resistivity and optical gap versus ion fluence of 40 keV argon-implanted PI. According to [11].

$$\sigma(T) = \sigma_0 \exp\left(-\left(T_0 / T\right)^m\right), \quad (1)$$

where σ_0 is the conductivity at temperature $T \to \infty$ and T_0 is the characteristic temperature. The power m is crucial for determining the conduction mechanism. For band conduction in extended states, m = 1. If states are not extended but Andersen localisation throughout the whole band so that any mobility edge is in a higher energy band, a nearest-neighbour hopping occurs which can also lead to a temperature dependence with m = 1 [102].

For a truly disordered material, Mott and Devis predicted a VRH mechanism between localised states [142]. For this mechanism m has following relation with the dimensionality D

$$m = 1/\left(1+D\right). \quad (2)$$

A three-dimensional (3D) VRH thus corresponds to m = 1/4. 2D and 1D models represent Eq. (1) with the power equal to 1/3 and 1/2, respectively. Majority of polymers implanted with low or medium fluences (10^{13}-10^{15} cm^{-2}) exhibit temperature dependence of conductance well described by Eq. (1) with m = 1/2 [57,135,138,139]. It was suggested [139] that 1D hopping mechanism dominates in this case. However, it is hard to believe that the disordered by implantation polymer can form the structures providing pure 1D conductance. Another possibility, suggested by Wang and co-authors [143], assumes that conduction along the ion tracks would be 1D in nature while conduction in the highly disordered region, around the mean ion range, may be 3D. This

model of the mixed conduction mechanisms gives reasonable agreement with the experimental results and allows calculating average characteristic temperatures and activation energies which are found to be decreasing functions of ion fluence.

With further fluence increase, the value of power *m* is observed to be decreasing to 1/3 or 1/4, for example, for PI implanted by N^+ and Ar^+ ions [52,140], PE and PA bombarded by B^+ and Sb^+ ions [90,144]. For the cases of *m* = 1/3 the formation of a quasi-2D electron gas in the buried carbonised layer was suggested [85]. Otherwise, 3D VRH dominates [52,144,145]. Several groups reported the conduction behaviour with *m* = 1 for the cases of either high-energy (MeV) [146] or high-fluence (10^{16} cm^{-2}) [147] implantation of polymers. It is also found that *m* value can be close to 1 (0.7-0.8) but does not reach it even for high fluences (10^{17} cm^{-2}) as for boron implantation into PE [90]. In this case the heavily carbonised layer can represent either the mechanism of conductance with constant activation energy or the nearest-neighbour hopping.

Current-voltage (*I-V*) dependences of the implanted polymers are typically found to be linear [90,148,149]. However, a hysteresis-like behaviour for *I-V* plots is observed for PE implanted with medium fluences (Fig. 19) [90]. This effect can be attributed to the aligning of the electric dipoles in the implanted layer by the applied electric field: the orientation of the dipoles being retained due to a relatively high resistivity of the layer. The occurrence of the dipole moments is related to the individual carbon clusters enriched by π-electrons and separated from each other by insulating barriers. With fluence increase over 1×10^{16} cm^{-2} the effect vanishes that is explained by overlapping of the carbonised inclusions. Similarly, no hysteresis effect was observed for implantation of 50 keV Si^+ ions into PMMA with fluencies $\geq 1\times10^{16}$ cm^{-2} [150].

Metal-implanted polymers represent a special case regarding the conductance. Typically, resistivity of the layer implanted by metal ions is lower compared to implantation of non-metal species with the same fluence. The lowest values are reported for the Cu- and Ag-implanted PET reaching 1.5×10^{-4} Ω·cm for the fluence of 2×10^{17} cm^{-2} [151]. Similar values of ca. 1×10^{-4} Ω·cm were measured for the streaming plasma implantation of gold into PMMA with dose of 3.2×10^{16} cm^{-2} [23]. For Au- and Ti-implanted PDMS the resistivity was shown to saturate near 1 kΩ/square for the fluencies above 2×10^{16} cm^{-2} [152]. Conversion of this value gives the bulk resistivity of 2.2×10^{-6} and 4.2×10^{-5} Ω·cm for gold and titanium, respectively. These examples

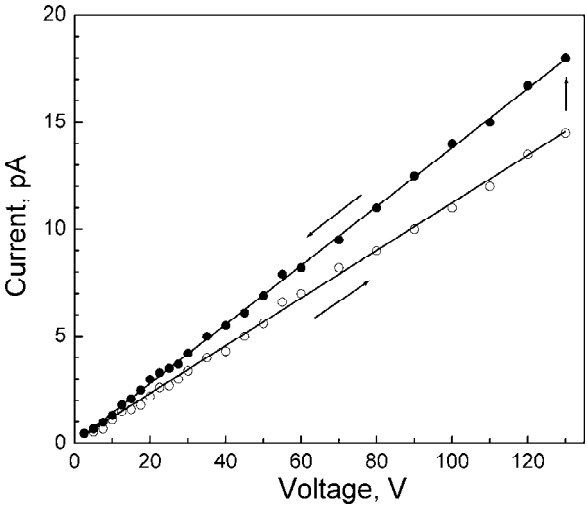

Fig. 19. Current-voltage dependence of PE implanted by 100 keV B^+ ions with fluence of 5×10^{15} cm^{-2}. According to [90].

allow assuming that in the polymers implanted with high-fluence metal ions electron transport can be caused by both the radiation-induced changes of the material and the filling with metal [153].

For PI implanted with high fluences (2.5×10^{16}-1.25×10^{17} cm^{-2}) of Co^+ ions at ion current density of 4 μA/cm^2 VRH is found to be dominating mechanism [21]. As can be seen in Fig. 20 the curves corresponding to the lowest fluences follow a linear function in co-ordinates R - $(1/T)^{1/4}$ but only in the high-temperature interval of the measurements. With fluence increase, the linear function with *m* = 1/4 extrapolates the experimental dependences down to $T \approx 40$K. Below this temperature, $R \sim (1/T)^{1/3}$ (Fig. 20, insertion). Co^+ ion implantation with a fluence of 1.25×10^{17} cm^{-2} at j = 8 and 12 μA/cm^2 leads to a significant change in the temperature dependence of resistance (Fig. 21). The dependence with a minimum which is shown in the figure is typical for disordered (granular) metal films. Calculation of a local activation energy using the method proposed in [154] allows suggesting metallic type of electron transport in these samples or, in other words, IMT due to agglomeration of Co NPs forming a percolation way for the charge carriers. It is shown that both quantum effects of weak localisation and electron-electron interaction give a significant contribution to the transport mechanism and conductivity can be described by the equation

$$\sigma(T) = \sigma_0 + AT^{1/2} + B\ln T, \qquad (3)$$

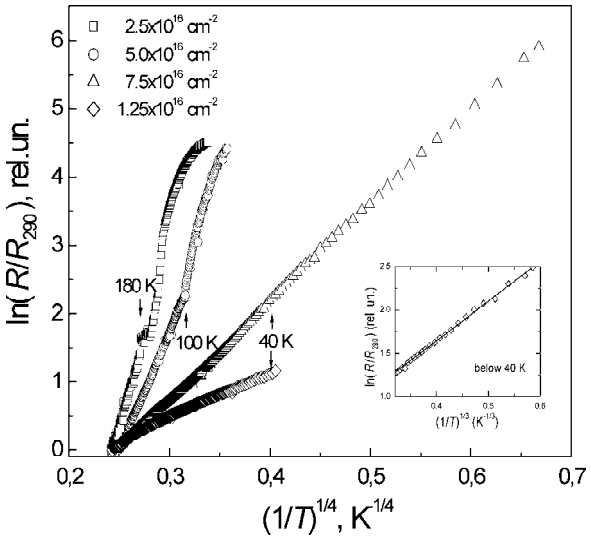

Fig. 20. Temperature dependence of resistance of PI implanted by 40 keV Co^+ ions with various fluences at ion current density of 4 μA/cm^2. The low-temperature interval for fluence 1.25×10^{17} cm^{-2} is in insertion. According to [21].

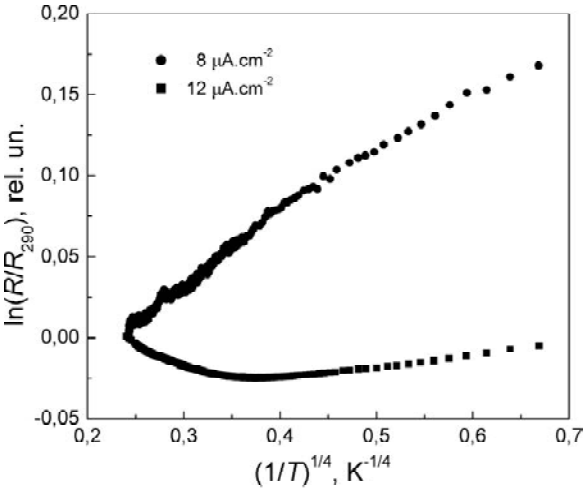

Fig. 21. Temperature dependence of resistance of PI implanted by 40 keV Co^+ ions with fluence of 1.25×10^{17} cm^{-2} at two different ion current densities. According to [21].

where *A* and *B* are the fit parameters. The IMT transition was also found for PET implanted by 40 keV Fe^+ ions with fluence of 1.0×10^{17} cm^{-2} at *j* = 4 μA/cm^2 [22].

According to commonly-accepted theories of electronic transport in isotropic percolating materials, the bulk conductivity of a metal/insulator composite near the IMT can be given by the power law

$$\sigma = \sigma_0 \left(\phi - \phi_C\right)^t, \quad (4)$$

where ϕ and ϕ_C are the normalised metal concentration and the critical concentration corresponding to the percolation, respectively. For the percolation regime, exponent *t* is predicted to be less than 2 [155]. Percolation threshold can vary significantly depending on the composites. In the literature, one can find ϕ_C between 0.01 and 0.5 [155]. For the above-mentioned cases of cobalt and iron implantation, ϕ_C was estimated to be about 0.20-0.25. Transition to percolation was demonstrated for low-energy implantation of Au and Ti in PDMS to high fluencies [152]. The percolation thresholds were measured to be as low as 0.06-0.08 for gold and 0.11-0.13 for Ti. For the streaming plasma ultra-shallow implantation of gold into PMMA, ϕ_C was determined at around 0.47 [23, 24].

Study of electrical properties of implantation-modified polymers is of significant importance for plastic electronics which is a forefront research area where organic semiconductors replace the present silicon based technology. Thus, conducting polymers are essential components to this field, as well as exhibiting other important properties applicable in photonics, chemical/biosensors and as bio-compatible materials [20]. Some of these applications will be mentioned in the next sections. Recently, it was demonstrated that variation of electrical conductance of shallow metal-implanted polymers as a function of the applied surface load can be used for strain gauge applications [25].

4.2. Optical properties

Implantation-induced alteration of polymer structure and composition changes optical properties. Optically transparent polymers acquire some colour after implantation [12]. The colour changes from pale yellow to deep brown or grey with the fluence increase; metallic lustre appears at high fluences (≥ 1×10^{15} cm^{-2}) [156]. This phenomenon is consistent with the red shift of the absorption edge as can be seen in Fig. 22. This shift is caused by the carbonisation, in particular, by the nanodimensional carbon-enriched clusters which were discussed in Section 2.2. Thus, analysis of optical spectra allows extracting the cluster size [85,88]. Assuming that finite carbon clusters are composed of some number of fused benzene rings the following relation derived for amorphous carbon [157] can be used:

$$E_g = 2|\beta|N^{-1/2}, \quad (5)$$

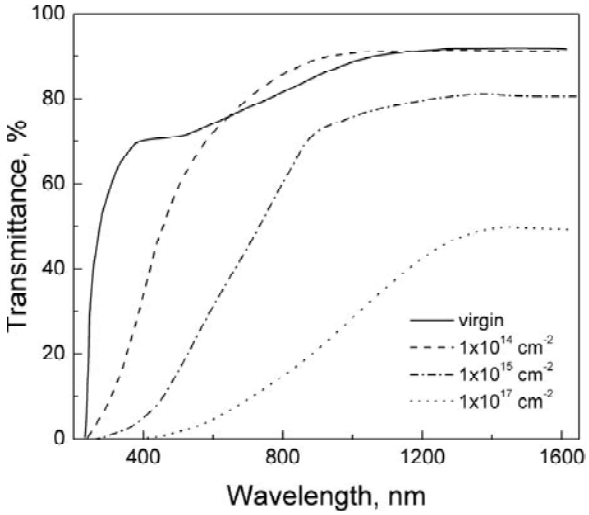

Fig. 22. Optical transmission spectra of PA implanted by 100 keV B^+ ions with different fluences. According to [88].

where E_g is the optical gap, which can be evaluated using the Tauc plot [158] for the optical spectrum, β is the resonance integral (Hückel theory gives β = 2.9) and N is the number of benzene rings forming the cluster. By known value of the optical gap one can extract the number of rings, i.e. approximate the cluster size. Optical gap decreases with ion fluence [67,150], i.e. with the increase of carbonisation but the gap value typically saturates at fluencies of (1-2)×10^{16} cm^{-2} as can be seen in Fig. 23. For the implanted PP [148], PS [159], PE [88,160], and PA [88] the saturation value was found to be about 0.6 eV. For the PC implanted by 50 keV

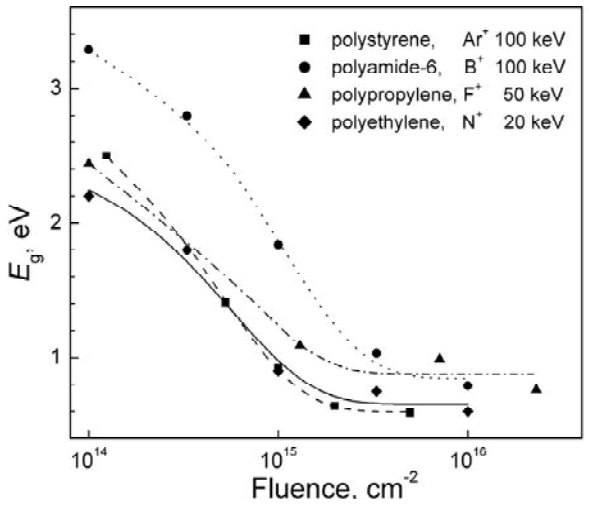

Fig. 23. Dependence of optical gap on ion fluence for various polymers implanted by different species and various energies. Conditions are indicated in the panel. According to [88,160,161].

Ar^+ ions with fluence of 1.2×10^{16} cm^{-2} the optical gap becomes as small as 0.4 eV [161]. According to Eq. (5) value of 0.6 eV corresponds to a carbon cluster comprising about 100 benzene rings, i.e. of ~2.0-2.5 nm in mean diameter [85,88]. This estimate is rough because the equation is valid only for compact clusters. Moreover, the Hückel theory can overestimate the energies of the optical transitions in the π-systems. Nevertheless, optical spectroscopy enables to trace the major stages of carbonaceous phase formation in implanted polymers. For example, the nucleation of smaller clusters (wider optical gap before saturation) for PA compared to other polymers (see Fig. 23) can be a result of incorporation of heteroatoms (nitrogen) into the clusters reducing the size of extended region of the π-electron conjugated system.

Change of optical gap for implanted polymers is in good correlation with the change of electrical resistance (as can be seen in Fig. 18) because both phenomena are strongly connected to the chemical and structural modification of the polymer. This correlation is found for variety of polymers and well illustrated, for instance, for the PI implanted by Ar with high-fluence and high ion current density [11]. At fluence of 1×10^{17} cm^{-2} the optical gap becomes as small as 0.25 eV. This value is close to that typical for amorphous carbon. From the correlation of optical, paramagnetic and electrical parameters it is suggested that the optical gap can approximately correspond to the band gap of the semiconducting material formed due to the polymer alteration under the implantation.

Optical parameters such as refractive index and extinction coefficient can be calculated from the absorption and reflection spectra of the implanted polymers [162]. They change significantly under irradiation: refractive index is essentially dependent on the implantation energy and it is increasing function of fluence [16,163]. For some polymers, the reflectivity increases by a factor of 5 after the implantation compared to non-implanted substrates [164]. It is worth noting that rather small fluences (10^{13}-10^{14} cm^{-2}) can be used for efficient control of optical parameters. Tuning the refractive index by implantation allows using this method for formation of planar waveguides in the polymer films. By masking technology or photolithography it is possible to make either surface or buried waveguides depending on the implantation energy [15,16]. The specimens of Y-branches and interferometers were produced (Fig. 24) [15]. Technology for formations of Mach-Zehnder modulator using reactive ion beam etching of PI was suggested [14]. The nonlinear

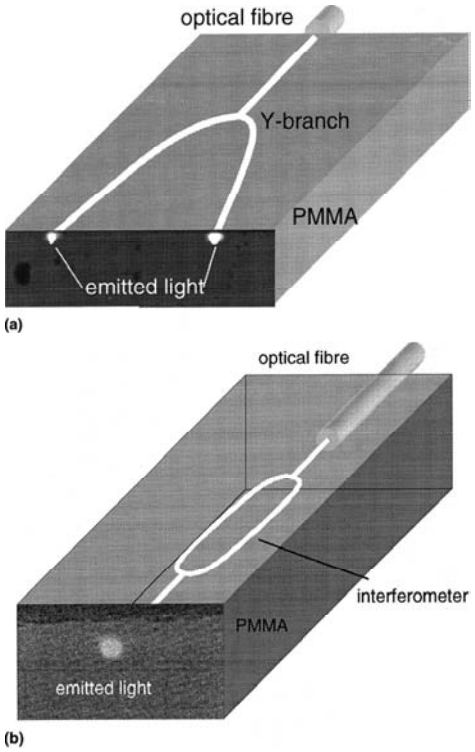

Fig. 24. Schematic pictures of (a) planar splitter and (b) Mach-Zehnder interferometer produced by high-energy implantation of C^+ ions with fluence of 1×10^{12} cm^{-2}. Reprinted from [15] with permission from Elsevier.

properties such as an electronic nonlinear refractive index and high values of a third-order susceptibility are expected for the implanted polymers due to the conjugation systems sharing π-electrons that could be highly polarizable and could lead to Kerr effect in an intense electric field [13].

Interesting results were shown on low-energy (30-50 keV) Si^+ ion implantation of PMMA [165]. The high-fluence embedding of Si leads to significant enhancement of photoluminescence (PL) of the polymer. As can be seen in Fig. 25, the PL intensity increases factor of 2-3 with the fluence rise for the samples implanted with energy of 30 keV. For the implantation energy of 50 keV and fluence of $1x10^{15}$ cm^{-2} an increase of PL intensity up to 5 times compared to the unimplanted samples was reported. However, it is not clear from the paper if the PL enhancement is mainly related to the formation of Si NPs.

Additionally to interest in reflectivity and photoluminescence of implanted polymers, the phenomenon of surface plasmon resonance (SPR) of metal NPs in organic-based media attracts considerable attention. SPR phenomenon gives rise to nonlinear

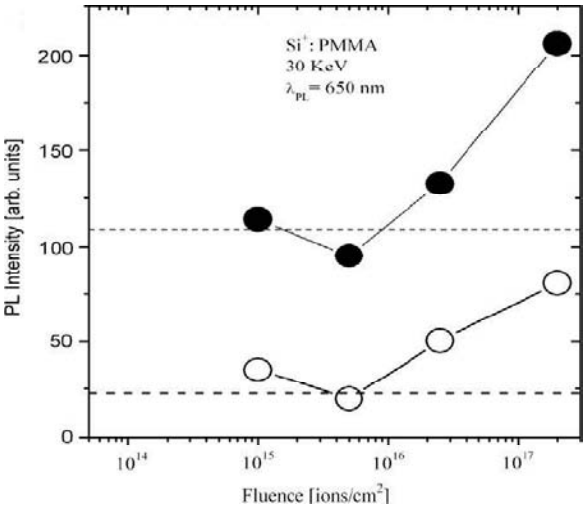

Fig. 25. Maximum PL intensity (at wavelength of 650 nm) versus implantation fluence of PMMA implanted by Si^+ ions with energy of 30 keV. Open symbols correspond to excitation by laser power of 10 mW, solid symbols – 30 mW. Dashed line shows PL intensity of unimplanted PMMA. Reprinted from [165] with permission from Elsevier.

optical effects, for instance, high nonlinear third-order susceptibility when exposed to ultra-short (ps or fs) laser pulses [26,166]. In practice, SPR effect may be enhanced by raising the nanoparticle concentration in the host matrix, i.e. by increasing the volume fraction of the metal phase (filling factor). Systems with a higher filling factor offer a higher nonlinear third-order susceptibility which is of interest for practical applications [166].

Noble metal NPs exhibit the most pronounced SPR effect and, hence, the highest nonlinearity of the NP optical properties in dielectrics. Such composite materials were fabricated by Ag-ion implantation into epoxy resins [119,167], PET [151,168] and PMMA [169]. Optical absorption spectra of PMMA irradiated by silver ions with various fluencies are presented in Fig. 26 [169]. For comparison, polymer samples were also implanted by Xe^+ ions. As seen in Fig. 26a, absorption of PMMA increases with xenon fluence due to the polymer carbonisation as discussed above. Implantation of Ag^+ ions not only causes the carbonisation but also leads to the formation of metal NPs. SPR bands can be clearly seen in Fig. 26b. For the lowest ion fluence, the maximum of this band is near 420 nm and it shifts towards longer wavelengths (up to ~550-600 nm) with fluence increasing. The shift is accompanied by the band

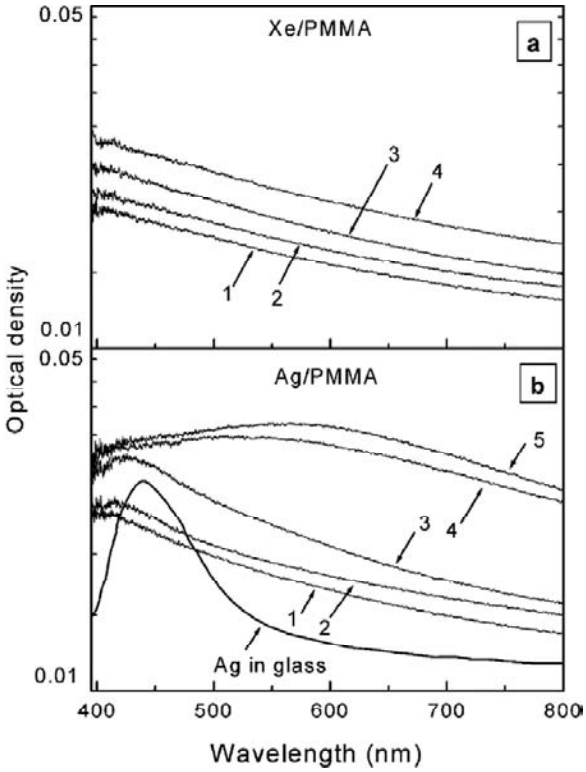

Fig. 26. Optical absorption spectra of PMMA implanted by (a) 30 keV Xe^+ and (b) Ag^+ ions with fluences of (1) 3×10^{15}, (2) 6×10^{15}, (3) 2.5×10^{16}, (4) 5×10^{16}, and (5) 7.5×10^{16} cm^{-2}. Spectra of unimplanted PMMA and silica glass with Ag NPs formed by implantation are presented for comparison. According to [169].

broadening. For the comparison, Fig. 26b also shows the spectrum for inorganic silica glass irradiated by silver ions under the same implantation conditions [170]. Particle size distributions in the SiO_2 and PMMA are nearly the same. SiO_2 has the refractive index close to that of PMMA. However, the band associated with Ag NPs in the glass is much more narrow and intense.

Very similar results for silver-implanted polymers are obtained by Boldyryeva et al. Ag^+ ion implantation with energy of 60 keV into PMMA and PC causes formation of NPs and characteristic SPR bands appear in the optical spectra [99,171]. These bands are pretty wide and they demonstrate the red shift of the maximum from ca. 2.6 eV to 2.2-2.3 eV (from ca. 475 to ca. 540-560 nm) with the fluence increase from $3x10^{16}$ to $3x10^{17}$ cm^{-2}. Cu^- ions implanted to high fluencies into high-density PE, PS, and PC also cause SPR bands in the spectra [172]. The bands are centred around 2 eV (ca. 620 nm). However, the band intensities are very low and one needs the fluencies $\geq 1x10^{17}$ cm^{-2} to resolve them. Therefore, it is difficult to say anything about the red shift.

To clarify the reasons of the SPR band shift and its broadening for the cases of silver implantation the modelling was carried out. Optical spectra of spherical metal NPs embedded in various dielectric media can be simulated in terms of the Mie electromagnetic theory (see for instance [173]), which allows one to estimate the extinction cross section σ_{ext} for a light incident on a particle. σ_{ext} can be represented as a sum of cross-sections related to the absorption σ_{abs} and elastic scattering σ_{sca}. It can be found from Lambert-Beer law

$$\Delta I = I_0\left(1-\exp\left(\frac{1}{n\sigma_{ext}h}\right)\right), \qquad (6)$$

where I_0 and ΔI are the intensity of the incident light and its loss, respectively, n is the density of NPs in the layer and h is its thickness. Optical density, OD, of the specimens can be found as $OD = -\lg(I/I_0)$.

Simulated extinction spectra of Ag NPs embedded in PMMA are shown in Fig. 27 [169]. This modelling reproduces rather well the experimental cases of low-fluences (curves 1-3 in Fig. 26b). For higher implantation fluences, the carbonisation must be considered. This situation was modelled by constructing the core-shell systems where the core is Ag NP and the shell is amorphous carbon. Optical extinction spectra of Ag NPs with a fixed size of the core (4 nm) and a varying thickness of the carbon shell (from 0 to 5 nm) are shown in Fig. 28 [169]. The maximum of SPR band shifts from 410 nm to approximately 510 nm with increase of the shell thickness. Simultaneously, the SPR band intensity decreases. This behaviour agrees with the evolution of experimental spectra at fluencies $\geq 2.5\cdot10^{16}$

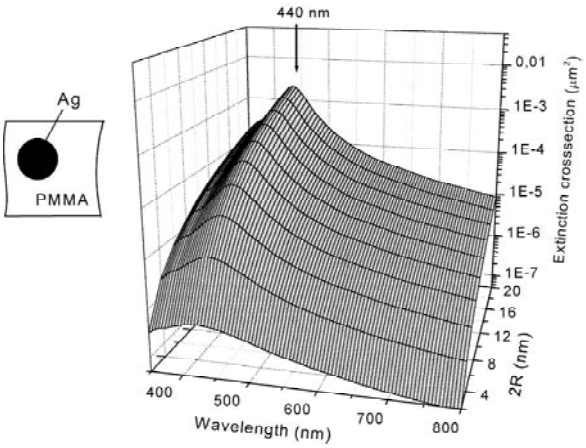

Fig. 27. Calculated extinction spectra of Ag NPs in PMMA as a function of particle size (2R means diameter). According to [169].

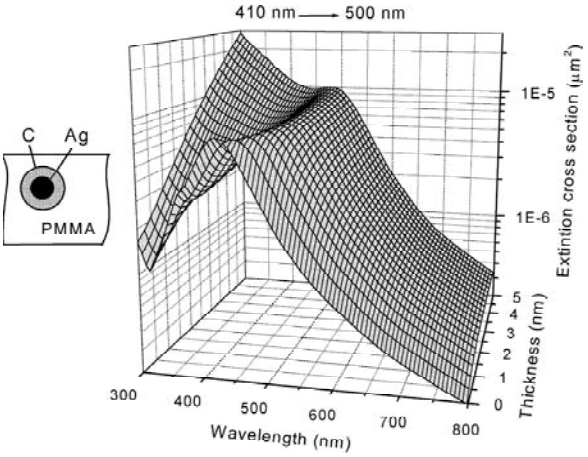

Fig. 28. Calculated extinction spectra of Ag NPs of fixed diameter (4 nm) covered by amorphous carbon shell in PMMA as a function of shell thickness. According to [169].

ion/cm^2 (see Fig. 26b). Qualitatively similar results were obtained for PI implanted by high fluencies of Au^+ ions [121]. Fig. 15 shows the formation of gold NPs in the shallow polymer layer. Modelling of the core-shell (Au-C) structures using Mie theory demonstrated a red shift of the SPR band and dumping of its intensity.

Thus, the cases of noble metal NPs in polymers are among those mostly studied for the SPR phenomenon. However, quite recently it was demonstrated that Ti NPs formed in PS matrix using plasma immersion ion implantation can also exhibit characteristic absorption band in UV region at 337 nm [174]. This study is of considerable interest because Ti NPs are important elements for the production of waveguide layers, optical filters and some other optical applications.

4.3. Magnetic properties

Pristine polymers are in most cases diamagnetic materials. Only some of them, for example, PI and poly(ether sulfone) reveal a weak signal of electron paramagnetic resonance (EPR) with $g = 2.0025$ due to a nonhomogeneous electron interaction caused by the heteroatoms in the polymer chain [57,175]. Ion implantation of polymers results in massive rupture of chemical bonds, formation of free radicals and conjugated systems associated with the carbonaceous phase. Therefore, electronic structure of the implanted layers undergoes significant change leading to the appearance of paramagnetic properties. EPR spectra of polymers implanted to moderate or high fluences typically show an isotropic singlet with *g*-value of 2.0025 which is close to that of free electron (2.0023) [2,73,134,139]. This value also coincides (within the error) with values of 2.0026 and 2.0027 that are characteristic of conducting and pyrolised polymers [176-178]. This fact indicates the similarity of paramagnetic centres in various carbon-based materials and for different methods of treatment. However, the radiation-damage-related change of the paramagnetic behaviour goes beyond the scope of this paper: more details on this topic can be found elsewhere [69]. Below, we mostly focus on the properties of metal-implanted polymers, in particular, on the change of the magnetic properties due to the embedding of ferromagnetic impurities. It is worth noting that investigation of magnetic properties of such systems is still under development. After first publications on ferromagnetic properties of metal-implanted polymers in the middle of the 80's [116,179] next generation of results on this subject showed up only in the middle of the 90's [180]. Since that time ferromagnetic properties of transition metal NPs synthesised in polymers by implantation has been under intensive study.

For the case of transition metals such as iron, cobalt or nickel, the ensemble of metal NPs formed in the implanted layer of polymer may behave as a thin layer of ferromagnetic continuum due to strong magnetic dipolar coupling between the particles. The magnetic percolation transition in this films may be observed by ferromagnetic resonance (FMR) measurements [32,33,124,181-183]. The transition occurs if concentration of the magnetic NPs is high enough and strength of the interparticle coupling is comparable with Zeeman energy of the NPs in the external magnetic field [35]:

$$\frac{m_i m_{i+1}}{r_{i,i+1}^3} \approx m_i H_{\text{mean}}, \tag{7}$$

where m_i is the magnetic moment of individual NP and r_i is the average distance between the NPs, $H_{\text{mean}} \sim 3300$ G is the mean resonance field of the individual magnetic NP. In the ferromagnetic continuum approximation the resonance field for two limiting orientations of the magnetic field with respect to the sample plane may be determined by Kittel's set of equations [184]:

$$\begin{aligned} h\nu &= g\mu \cdot \left(H_r - 4\pi M\right) \quad \theta_H = 0^\circ, \\ h\nu &= g\mu \cdot \sqrt{H_r \cdot \left(H_r + 4\pi M\right)} \quad \theta_H = 90^\circ, \end{aligned} \tag{8}$$

where h is Plank constant, ν is the resonance frequency, H_r is the resonance magnetic field, μ is

Bohr magneton and *M* is the magnetisation for two orientations of plane of the implanted layer, parallel ($\theta_H = 0^o$) and perpendicular ($\theta_H = 90^o$), in respect to the magnetic field. These equations give a possibility to extract both the *g*-value and magnetisation.

For the iron-implanted polymers the effective *g*-value is calculated to be 2.1±0.1 which is close to typical *g*-value of bulk iron film [35]. For the Fe-implanted silicone polymer, PET and PI, the FMR signal was found for the fluences $\geq 2.5\times10^{16}$ cm^{-2} that correlates with the TEM data on the NPs nucleation. Intensity of the signal increases with fluence (Fig. 29) while the spectra gains strong anisotropy [123]. The resonance line shifts to low- or high-field range depending on the sample orientation in the magnetic field and amplitude of the signal changes non-monotonically. The phenomenon qualitatively resembles the anisotropy behaviour of the FMR signal of the continuous thin magnetic films, where the value of resonance field depends on the film orientation in the magnetic field [185]. Measurements of angular dependence of the effective anisotropy allow concluding that the iron-implanted polymers exhibit uniaxial out-of-plane type of anisotropy; magnetisation of the composite layer is directed in plane with the surface [35]. From the hysteresis behaviour of FMR spectra for the polymers implanted by Fe^+ ions a remanent magnetisation values were found for room temperature (Fig. 29) [35,123,128]. These graphs give an estimate of magnetic percolation transition for fluencies above 6.0×10^{16} cm^{-2}. Temperature-dependent SQUID measurements of the iron-implanted PET clearly showed transitions between the ferromagnetic and superparamagnetic states [186]. For fluence of 5.0×10^{16} cm^{-2}, the blocking temperature T_b was found to be ca. 30K. Above this temperature, the samples are in the superparamagnetic state. With fluence increase T_b increases too that corresponds to larger sizes of NPs and higher metal filling factor. Samples implanted with fluencies $\geq 1.0\times10^{17}$ cm^{-2} demonstrate pure ferromagnetic behaviour in a whole temperature range. Magnetoresistive measurements show good correlation between the electrical and magnetic properties of these samples in terms of percolation of the nucleated iron NPs at fluences above 7.5×10^{16} cm^{-2} [22]. This finding agrees quite well with the estimation of the magnetic percolation transition shown in Fig. 29 for different types of polymers.

Magnetic response of Co NPs synthesised by implantation in polymers is much weaker compared to the Fe ones. The cobalt-epoxy nanocomposites

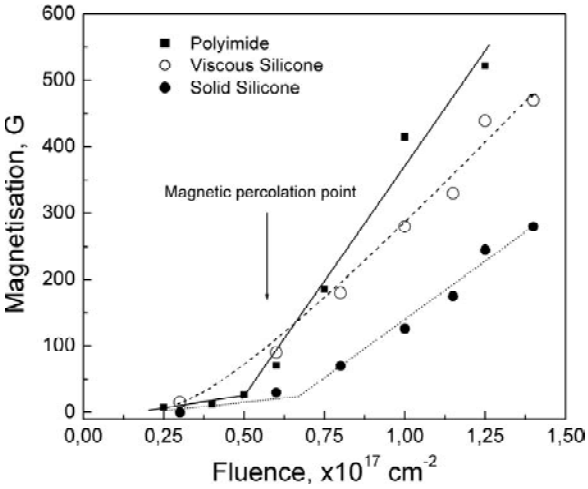

Fig. 29. Dependence of magnetisation on ion fluence for various polymers implanted by 40 keV Fe^+ ions. According to [35].

show the FMR signal for implantation fluences as high as 1.8×10^{17} cm^{-2} at ion current density of 4 μA/cm^2 [132,181]. Co-implanted PI represents the ferromagnetic properties only after subsequent thermal annealing or for the case of implantation at high ion current densities (8 and 12 μA/cm^2) [34] which is a sort of equivalence to annealing. The granular metal layer in the as-implanted sample consists of small cobalt NPs in a superparamagnetic state at room temperature. Orientation of the magnetic moments of the particles is affected by thermal fluctuations. Hence, the signal of magnetic resonance can be observed only if the frequency of the fluctuations decreases below the magnetic resonance frequency, i.e. at low temperatures. Indeed, FMR signal was found for samples implanted with fluences of 1.25×10^{17} and 1.50×10^{17} cm^{-2} at ion current density of 4 μA/cm^2 at low temperature of 100K. FMR signal for the annealed samples can be explained by coagulation and coalescence of the cobalt granules. The magnetic moments of these agglomerated particles are strongly magnetically coupled to each other [187]. Thus, the "effective magnetic" size of the agglomerates exceeds a critical size beyond which orientations of the magnetic moments are nearly static compared to the magnetoresonance measurement time. FMR study is in good agreement with the magnetoresistance measurements showing "positive" magnetoresistive effect (dielectric side of IMT) for PI samples implanted with fluence of $1.25\text{x}10^{17}$ cm^{-2} at ion current density of 4 μA/cm^2 while the samples implanted with the same fluence but at higher ion currents (8 and 12

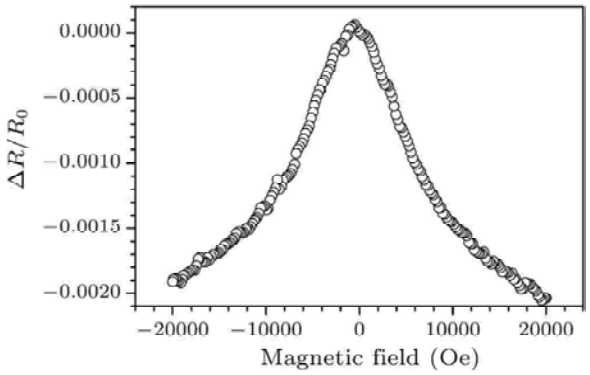

Fig. 30. Dependence of magnetoresistance on induction of magnetic field for PI implanted with $1.25x10^{17}$ and $1.75x10^{17}$ cm^{-2}. Reprinted with permission from [189]. © 2009, IOP Publishing.

μA/cm^2) leading to higher temperatures demonstrate "negative" magnetoresistive effect corresponding to metallic side of IMT [188]. "Negative" magnetoresistive effect is also found by Tian-Xiang et al. for the similar implantation conditions of cobalt into PI, see Fig. 30 [189].

5. CONCLUSIONS

Ion implantation is a powerful and versatile tool for modification of polymers. Control of the implantation energy, fluence and ion specie is key point for the obtaining of materials with required parameters. One also needs a clear understanding of physical processes taking place in polymers under the implantation. The paper presents a systematic analysis of numerous data on various aspects of ion bombardment of organic materials. This analysis covers the structural and compositional changes of polymers which are represented in terms of complex radiothermolysis phenomenon. The importance to consider carbonisation processes is especially emphasised.

Reviewing the studies on distribution of the implanted species shows that one needs to consider dynamical change of the polymer composition and structure as well as diffusion of the impurities in order to correctly predict the final depth profiles. Nucleation of metal nanoparticle is a special case of high-fluence implantation of metal ions. The nanoparticle formation is governed by the local metal concentration and metal diffusion coefficient as well as by parameters of the polymer material such as density, composition and viscosity.

Structural and composition alterations of the implanted polymer layers result in drastic change of chemical and physical properties. For instance, tuning the polymer conductance by ion implantation is of great importance. Polymer materials can be used as active elements of electronic devices. Disadvantage of the radiation-modified polymers is in low mobility of charge carriers. However, low prices and specific properties as plasticity and suppleness as well as stable dependence of the conductance on temperature give them an advantage to be used for fabrication of resistors, varistors and temperature sensors [4]. Formation of the buried carbonaceous conductive layer in the polymer matrix by means of implantation demonstrates a possibility to fabricate transistor-like electronic switches operating in AC mode [90]. By utilising the piesoresistive properties of the implanted polymers the strain gauges were produced [25,190].

Control of optical properties of polymers by implantation gives an impulse for fabrication of passive optical devises such as filters, waveguides, coatings for lenses etc. The synthesis of metal particles in polymer media by ion implantation opens a new area of materials science with perspectives for nanophotonics, plasmonics and non-linear optics. Polymer composites containing metal nanoparticles can also be used as gas and humidity sensors [191, 192]. Modification of surfaces and formation of the specific centres allows introducing the implantation-modified polymers into biology and medicine ranging from biocompatible materials to biosensors and biological devices [20].

Thus, both the capability of ion implantation technique and the acquired knowledge of physical and chemical processes accompanying implantation demonstrate good perspectives for practical utilisation of radiation-modified organic materials and metal/polymer nanocomposites.

ACKNOWLEDGEMENTS

The author is grateful to Dr. A.L. Stepanov from Kazan Physical-Technical Institute of RAS for the valuable discussions especially on the part about optical properties of nanoparticle systems.

REFERENCES

[1] C.K. Chiang, C.R. Fincher, Jr., Y.W. Park, A.J. Heeger, H. Shirakawa, E.J. Louis, S.C. Gau and A.G. MacDiarmid // *Phys. Rev. Lett.* **39** (1977) 1098.

[2] T. Venkatesan, L. Calcagno, B.S. Elman and G. Foti, In: *Ion Beam Modification of Insulators*, ed. by P. Mazzoldi and G.W. Arnold (Elsevier: Amsterdam, 1987), p. 301.
[3] G. Marletta and F. Iacona, In: *Materials and Processes for Surface and Interface Engineering*, ed. by Y. Pauleau (Kluwer, Dordrecht, 1995), p. 597.
[4] R.E. Gied, M.G. Moss, J. Kaufmann and Y.Q. Wang, In: *Electrical and Optical Polymer Systems*, ed. by D.L. Wise, G.E. Wnek, D.J. Trantolo, T.M. Cooper and J.D. Gresser (Marcel Dekker: New York, 1998), p. 1011.
[5] A. Chapiro // *Nucl. Instrum. Meth. Phys. Res. B* **32** (1988) 111.
[6] D.V. Sviridov, V.B. Odzhaev and I.P. Kozlov, In: *Electrical and Optical Polymer Systems*, ed. by D.L. Wise, G.E. Wnek, D.J. Trantolo, T.M. Cooper and J.D. Gresser (Marcel Dekker, New York, 1998), p. 387.
[7] V.N. Popok // *Surf. Investigations* **14** (1999) 843.
[8] E.H. Lee // *Nucl. Instrum. Meth. Phys. Res. B* **151** (1999) 29.
[9] D.V. Sviridov // *Rus. Chem. Rev.* **71** (2002) 315.
[10] M. Iwaki // *Nucl. Instrum. Meth. Phys. Res. B* **175-177** (2001) 368.
[11] V.N. Popok, I.I. Azarko, R.I. Khaibullin, A.L. Stepanov, V. Hnatowicz, A. Mackova and S.V. Prasalovich // *Appl. Phys. A* **78** (2004) 1067.
[12] D. Fink, M. Muller, L.T. Chadderton, P.H. Cannington, R.G. Elliman and D.C. McDonald // *Nucl. Instrum. Meth. Phys. Res. B* **32** (1988) 125.
[13] P. Cottin, R.A. Lessard, E.J. Knystautas and S. Roorda // *Nucl. Instrum. Meth. Phys. Res. B* **151** (1999) 97.
[14] A. Moliton, R. Antony, B. Lucas, B. Ratier and C. Moussant // *Opt. Mater*. **12** (1999) 199.
[15] D.M. Rück // *Nucl. Instrum. Meth. Phys. Res. B* **166-167** (2000) 602.
[16] F.F. Komarov, A.V. Leontyev, V.V. Grigoryev and M.A. Kamishan // *Nucl. Instrum. Meth. Phys. Res. B* **191** (2002) 728.
[17] J.D. Carlson, J.E. Bares, A.M. Guzman and P.P. Pronko // *Nucl. Instrum. Meth. Phys. Res. B* **7/8** (1985) 507.
[18] Y. Suzuki // *Nucl. Instrum. Meth. Phys. Res. B* **206** (2003) 228.
[19] A. Kondyurin, B.K. Gan, M.M.M. Bilek, D.R. McKenzie, K. Mizuno and R. Wuhrer // *Nucl. Instrum. Meth. Phys. Res. B* **266** (2008) 1074.
[20] G. Marletta, In: *Materials Science with Ion Beams, Topics Appl. Phys. 116*, ed. by H. Bernas (Springer-Verlag: Berlin, 2010), p. 345.
[21] V.N. Popok, M.G. Lukashevich, S.M. Lukashevich, R.I. Khaibullin and V.V. Bazarov // *Surf. Sci.* **566-568** (2004) 327.
[22] M.G. Lukashevich, V.N. Popok, V.S. Volobuev, A.A. Melnikov, R.I. Khaibullin, V.V. Bazarov, A. Wieck and V.B. Odzhaev // *Open Appl. Phys. J.* **3** (2010) 1.
[23] F.S. Teixeira, M.C. Salvadori, M. Cattani and I.G. Brown // *J. Appl. Phys.* **105** (2009) 064313.
[24] F.S. Teixeira, M.C. Salvadori, M. Cattani and I.G. Brown // *J. Appl. Phys.* **106** (2009) 056106.
[25] G. Di Girolamo, M. Massaro, E. Piscopiello and L. Tapfer // *Nucl. Instrum. Meth. Phys. Res. B* **268** (2010) 2878.
[26] U. Kreibig and M. Vollmer, *Optical Properties of Metal Clusters* (Springer, Berlin, 1995).
[27] Ch. Buhal, S.P. Withrow, C.W. White and D.B. Poker // *Annu. Rev. Mater. Sci.* **24** (1994) 125.
[28] A.L. Stepanov // *Techn. Phys.* **49** (2004) 143.
[29] A.L. Stepanov, In: *Metal-Polymer Nanocomposites*, ed. by L. Nicolais and G. Garotenuto (J. Wiley&Sons: Hoboken, 2005), p. 241.
[30] A.L. Stepanov // *Rev. Adv. Mater. Sci.* **26** (2010) 1.
[31] S.A. Maier, P.G. Kik, L.A. Sweatlock and H.A. Atwater // *Mater. Res. Soc. Symp. Proc.* **777** (2003) T7.1.1.
[32] V.Yu. Petukhov, N.R. Khabibullina, M.I. Ibragimova, A.A. Bukharaev, D.A. Biziaev, E.P. Zheglov, G.G. Gumarov and R. Müller // *Appl. Magn. Reson.* **32** (2007) 345.
[33] R.I. Khaibullin, V.A. Zhikharev, Yu.N. Osin, E.P. Zheglov, I.B. Khaibullin, B.Z. Rameev and B. Aktas // *Nucl. Instrum. Meth. Phys. Res. B* **166-167** (2000) 897.
[34] B. Rameev, C. Okay, F. Yildizm R.I. Khaibullin, V.N. Popok and B. Aktas // *J. Magnet. Magn. Mater.* **278** (2004) 164.
[35] R.I. Khaibullin, B.Z. Rameev, C.Okay, A.L. Stepanov, V.A. Zhikharev, I.B. Khaibullin, L.R. Tagirov and B. Aktas, In: *Nanostructured*

Magnetic Materials and Their Applications, NATO Science Series: II Mathematics, Physics and Chemistry, V. 143, ed. by B. Aktas, L. Tagirov and F. Mikailov (Kluwer: Dordrecht, 2004), p.33.
[36] M.G. Lukashevich, X. Batlle, A. Labarta, V.N. Popok, V.A. Zhikharev, R.I. Khaibullin and V.B. Odzhaev // *Nucl. Instrum. Meth. Phys. Res. B* **257** (2007) 589.
[37] D. Fink, In: *Fundamentals of Ion-Irradiated Polymers,* ed. by D. Fink (Springer: Berlin, 2004), p. 171.
[38] R. Sudowe, P. Valter, R. Brandt, J. Vetter and W. Ensinger // *Nucl. Instrum. Meth. Phys. Res. B* **175-177** (2001) 564.
[39] A.I. Vilensky, O.G. Larionov, R.V. Gainutdinov, A.L. Tolstikhina, V.Ya. Kabanov, D.L. Zagorski, E.V. Khataibe, A.N. Netchaev and B.V. Mchedlishvili // *Rad. Measur.* **34** (2001) 75.
[40] R.M. Papaleo, In: *Fundamentals of Ion-Irradiated Polymers,* ed. by D. Fink (Springer: Berlin, 2004), p. 207.
[41] P. Apel, A. Schulz, R. Spohr, C. Trautmann and V. Vutsadakis // *Nucl. Instrum. Meth. Phys. Res. B* **131** (1997) 55.
[42] V. Hnatowicz // *Phys. Stat. Sol. (b)* **216** (1999) 931.
[43] H. De Cicco, G. Saint-Martin, M. Alurralde, O.A. Bernaola and A. Filevich // *Nucl. Instrum. Meth. Phys. Res. B* **173** (2001) 455.
[44] F. Seitz and J. Koehler, In: *Solid State Physics: Advances in Research and Applications*, V. 2, edited by F. Seitz and D. Turnbull (Academic: New York, 1956), p. 305.
[45] P. Sigmund // *Appl. Phys. Lett.* **25** (1974) 169.
[46] R. Kelly // *Rad. Eff.* **32** (1977) 91.
[47] I.S. Bitensky, P. Demirev and B.U.R. Sundquist // *Nucl. Instrum. Meth. Phys. Res. B* **82** (1993) 356.
[48] M. Behar and D. Fink, In: *Fundamentals of Ion-Irradiated Polymers,* ed. by D. Fink (Springer: Berlin, 2004), p. 119.
[49] J. F. Ziegler, J. P. Biersack, M. D. Littmark, *The Stopping and Ranges of Ions in Matter* (Lulu Press, Morrisville, 2008).
[50] J.L. Magee and A. Chattejee // *J. Phys. Chem.* **84** (1980) 3529.
[51] J. Davenas, X.L. Xu, G. Boiteux and D. Sage // *Nucl. Instrum. Meth. Phys. Res. B* **39** (1989) 754.
[52] V. Švorčik, R. Endršt, V. Rybka, E. Arenholz, V.Hnatowicz and F. Černy // *Eur. Polym. J.* **31** (1995) 189.
[53] M.B. Lewis and E.H. Lee // *Nucl. Instrum. Meth. Phys. Res. B* **61** (1991) 457.
[54] G. Marletta // *Nucl. Instrum. Meth. Phys. Res. B* **46** (1990) 295.
[55] V. Švorčik, R. Endršt, V. Rybka, V. Hnatowicz and F. Černy // *J. Electrochem. Soc.* **141** (1994) 582.
[56] V. Picq, J.M. Ramillon and E. Balanzat // *Nucl. Instrum. Meth. Phys. Res. B* **146** (1998) 496.
[57] L.B. Bridwell, R.E. Giedd, W. Youngqiang, S.S. Mohite, T. Jahnke and I.M. Brown // *Nucl. Instrum. Meth. Phys. Res. B* **59/60** (1991) 1240.
[58] G. Marletta and F. Iacona // *Nucl. Instrum. Meth. Phys. Res. B* **80/81** (1993) 1405.
[59] J. Davenas, I. Stevenson, N. Celette, S. Cambon, J.L. Gardette, A. Rivaton and L. Vignoud // *Nucl. Instrum. Meth. Phys. Res. B* **191** (2002) 653.
[60] L. Calcagno, R. Percolla and G. Foti // *Nucl. Instrum. Meth. Phys. Res. B* **95** (1995) 59.
[61] A. Licciardello, O. Puglisi, L. Cacagno and G. Foti // *Nucl. Instrum. Meth. Phys. Res. B* **32** (1988) 131.
[62] A. Licciardello, M.E. Fragala, G. Compagnini and O. Puglisi // *Nucl. Instrum. Meth. Phys. Res. B* **122** (1997) 589.
[63] T. Steckenreiter, E. Balanzat, H. Fuess and C. Trautmann // *Nucl. Instrum. Meth. Phys. Res. B* **151** (1999) 161.
[64] M. Eßer and J. Fuhrmann // *Nucl. Instrum. Meth. Phys. Res. B* **151** (1999) 118.
[65] V. Picq and E. Balanzat // *Nucl. Instrum. Meth. Phys. Res. B* **151** (1999) 76.
[66] A. Mackova, J. Bocan, R.I. Khaibullin, V.F. Valeev, P. Slepicka, P. Sajdl and V. Svorcik // *Nucl. Instrum. Meth. Phys. Res. B* **267** (2009) 1549.
[67] T. Sharma, S. Aggarwal, A. Sharma, S. Kumar, D. Kanjilal, S.K. Deshpande and P.S. Goyal // *J. Appl. Phys.* **102** (2007) 063527.
[68] V.N. Popok, R.I. Khaibullin, A. Toth, V. Beshliu, V. Hnatowicz and A. Mackova // *Surf. Sci.* **532-535** (2003) 1034.
[69] V.N. Popok, In: *Surface Science Research*, ed. by C.P. Norris (Nova Science Publ.: New York, 2005), p. 147.

[70] V. Hnatowicz, J. Kvitek, V. Švorčik and V. Rybka // *Eur. Polym. J.* **29** (1993) 1255.
[71] V. Hnatowicz, J. Kvitek, V. Švorčik and V. Rybka // Appl. Phys. A **58** (1994) 349.
[72] V. Hnatowicz, J. Kvitek, V. Švorčik, V. Rybka and V. Popok // *Czech. J. Phys.* **44** (1994) 621.
[73] I.I. Azarko, V. Hnatowicz, I.P. Kozlov, E.I. Kozlova, V.B. Odzhaev and V.N. Popok // *Phys. Stat. Sol. (a)* **146** (1994) K23.
[74] G.-H. Wang, G.-Q. Pan, L. Dou, R.-X. Yu, T. Zhang, S.-G. Jiang and Q.-L. Dai // *Nucl. Instrum. Meth. Phys. Res. B* **27** (1987) 410.
[75] O.N. Tretinnikov and Y. Ikada // *J. Polym. Sci.* **36** (1998) 715.
[76] V.B. Odzhaev, I.I. Azarko, I.A. Karpovich, I.P. Kozlov, V.N. Popok, D.V. Sviridov, V. Hnatowicz, O.N. Jankovskij, V. Rybka and V. Švorčik // *Mater. Lett.* **23** (1995) 163.
[77] V. Hnatowicz, V. Peřina, V. Havranek, V. Voseček, J. Novotny, J. Vacik, V. Švorčik, V. Rybka and A. Kluge // *Nucl. Instrum. Meth. Phys. Res. B* **161-163** (2000) 1099.
[78] V. Hnatowicz, V. Havranek, J. Kvitek, V. Peřina, V. Švorčik and V. Rybka // *Nucl. Instrum. Meth. Phys. Res. B* **80/81** (1993) 1059.
[79] V. Hnatowicz, J. Kvitek, V. Švorčik, V. Rybka, and V. Popok // *J. Appl. Polym. Sci.* **55** (1995) 451.
[80] O. Jankovskij, V. Švorčik, V. Rybka, V. Hnatowicz and V. Popok // *Nucl. Instrum. Meth. Phys. Res. B* **95** (1995) 192.
[81] V. Hnatowicz, J. Vacik, V. Švorčik, V. Rybka, V. Popok, O. Jankovskij, D. Fink and R. Klett // *Nucl. Instrum. Meth. Phys. Res. B* **114** (1996) 81.
[82] V. Hnatowicz, J. Vacik, J. Červena, V. Švorčik, V. Rybka, D. Fink and R. Klett // *Phys. Stat. Sol. (a)* **159** (1997) 327.
[83] V. Hnatowicz, J. Kvitek, V. Peřina, V. Švorčik, V. Rybka and V. Popok // *Nucl. Instrum. Meth. Phys. Res. B* **93** (1994) 282.
[84] V.N. Popok, I.I. Azarko, V.B. Odzhaev, A. Toth and R.I. Khaibullin // *Nucl. Instrum. Meth. Phys. Res. B* **178** (2001) 305.
[85] V.N. Popok, V.B. Odzhaev, I.P. Kozlov, I.I. Azarko, I.A. Karpovich and D.V. Sviridov // *Nucl. Instrum. Meth. Phys. Res. B* **129** (1997) 60.
[86] G.R. Rao, Z.L. Wang and E.H. Lee // *J. Mater. Res.* **8** (1993) 927.
[87] D. Fink, K. Ibel, P. Goppelt, V. Biersack, L. Wang and M. Behar // *Nucl. Instrum. Meth. Phys. Res. B* **46** (1990) 342.
[88] I.P. Kozlov, V.B. Odzhaev, I.A. Karpovich, V.N. Popok and D.V. Sviridov // *J. Appl. Spectr.* **65** (1998) 390.
[89] N. Shekhawat, S. Aggarwal, A. Sharma, S.K. Sharma, S.K. Deshpande and K.G.M. Nair // *J. Appl. Phys.* **109** (2011) 083513.
[90] V.N. Popok, I.A. Karpovich, V.B. Odzhaev and D.V. Sviridov // *Nucl. Instrum. Meth. Phys. Res. B* **148** (1999) 1106.
[91] R. Nathawat, Y.K. Vijay, P. Kumar, P. Kulriya, V. Ganesan and V. Sathe // *Adv. Polymer Technol.* **27** (2008) 143.
[92] F. Schwarz, G. Thorwarth and B. Stritzker // *Sol. State Sci.* **11** (2009) 1819.
[93] R.B. Guimaraes, M. Behar, R.P. Livi, J.P. de Souza, L. Amaral, F.C. Zawislak, D. Fink and J.P. Biersack // *Nucl. Instrum. Meth. Phys. Res. B* **19/20** (1987) 882.
[94] M. Behar, P.L. Grande, L. Amaral, J.R. Kaschny, F.C. Zawislak, R.B. Guimaraes, J.P. Biersack and D.Fink // *Phys. Rev. B* **41** (1990) 6145.
[95] V. Hnatowicz, J. Vacik, J. Červena, V. Peřina, V. Švorčik and V. Rybka // *Nucl. Instrum. Meth. Phys. Res. B* **136-138** (1998) 568.
[96] G. Zhou, R. Wang and T.H. Zhang // *Nucl. Instrum. Meth Phys. Res. B* **268** (2010) 2698.
[97] W. Möller, W. Eckstein and J.P. Biersack // *Comput. Phys. Commun.* **51** (1988) 355.
[98] A.L. Stepanov, V.A. Zhikharev, D.E. Hole, P.D. Townsend and I.B. Khaibullin // *Nucl. Instrum. Meth. Phys. Res. B* **166-167** (2000) 26.
[99] H. Boldyryeva, N. Umeda, O.A. Plaksin, Y. Takeda and N. Kishimoto // *Surf. Coat. Technol.* **196** (2005) 373.
[100] P. Malinsky, A. Mackova, V. Hnatowicz, R.I. Khaibullin, V.F. Valeev, P. Slepička, V. Švorčik, M. Slouf and V. Peřina // *Nucl. Instrum. Meth. Phys. Res. B* **272** (2012) 396.
[101] R.B. Guimaraes, L. Amaral, M. Behar, F.C. Zawislak and D. Fink // *Nucl. Instrum. Meth. Phys. Res. B* **39** (1989) 800.
[102] Y. Wang, S.S. Mohite, L.B. Bridwell, R.E. Giedd and C.J. Sofield // J. Mater. Res. **8** (1993) 388.
[103] J.M. Colwell, E. Wentrup-Byrne, J.M. Bell and L.S. Wielunski // *Surf. Coat. Technol.* **168** (2003) 216.

[104] D. Fink, J.P. Biersack, J.T. Chen, M. Stadele, K. Tjan, M. Behar, C.A. Olovieri and F.C. Zawislak // *J. Appl. Phys.* **58** (1985) 668.
[105] R.B. Guimaraes, M. Behar, R.P. Livi, J.P. de Souza, F.C. Zawislak, D. Fink and J.P. Biersack // *J. Appl. Phys.* **60** (1986) 1322.
[106] D. Fink, M. Behar, J. Kaschny, R. Klett, L.T. Chadderton, V. Hnatowicz, J. Vacik and L. Wang // *Appl. Phys. A* **62** (1996) 359.
[107] M. Behar, P.F.P. Fichter, P.L. Grande and F.C. Zawislak // *Mater. Sci. Eng. R* **15** (1995) 1.
[108] J. Vacik, J. Červena, D. Fink, R. Klett, V. Hnatowicz, V. Popok and V. Odzhaev // *Rad. Eff. Def. Sol.* **143** (1997) 139.
[109] V.N. Popok, R.I. Khaibullin, V.V. Bazarov, V.F. Valeev, V. Hnatowicz, A. Mackova and V.B. Odzhaev // *Nucl. Instrum. Meth. Phys. Res. B* **191** (2002) 695.
[110] G.R. Rao, K. Monar, E.H. Lee and J.R. Treglio // *Surf. Coat. Technol.* **64** (1994) 69.
[111] J. Zhang, X. Ye, X. Yu and H. Li // *Mater. Sci. Eng. B* **84** (2001) 200.
[112] S.N. Abdullin, A.L. Stepanov, Yu.N. Osin and I.B. Khaibullin // *Surf. Sci.* **395** (1998) L242.
[113] M. Quinten, A. Heilmann and A. Kiesow // *Appl. Phys. B* **68** (1999) 707.
[114] J. Davenas, A. Perez, P. Thevenard and C.H.S. Dupuy // *Phys. Stat. Sol. (a)* **19** (1973) 679.
[115] G.W. Arnold // *J. Appl. Phys.* **46** (1975) 4466.
[116] N.C. Koon, D. Weber, P. Pehrsson and A.I. Schindler // *Mater. Res. Soc. Symp. Proc.* **27** (1984) 445.
[117] P.E. Pehrsson, D.C. Weber, N.C. Koon, J.E. Campana and S.L. Rose // *Mater. Res. Soc. Symp. Proc.* **27** (1984) 429.
[118] T. Kobayashi, T. Iwata, Y. Doi and M. Iwaki // *Nucl. Instrum. Meth. Phys. Res. B* **175-177** (2001) 548.
[119] A.L. Stepanov, S.N. Abdullin, R.I. Khaibullin, V.F. Valeev, Yu.N. Osin, V.V. Bazarov and I.B. Khaibullin // *Mater. Res. Soc. Symp. Proc.* **392** (1995) 267.
[120] V.Yu. Petukhov, M.I. Ibragimova, N.R. Khabibullina, S.V. Shulyndin, Yu.N. Osin, E.P. Zheglov, T.A. Vakhonina and I.B. Khaibullin // *Polym. Sci., Ser. A* **43** (2001) 1154.
[121] G. Maggioni, A. Vomiero, S. Carturan, et al. // *Appl. Phys. Lett.* **85** (2004) 5712.
[122] M. Niklaus, S. Rosset, M. Dadras, P. Dubois and H. Shea // *Scripta Mater.* **59** (2008) 893.
[123] R.I. Khaibullin, V.N. Popok, V.V. Bazarov, E.P. Zheglov, B.Z. Rameev, C. Okay, L.R. Tagirov and B. Aktas // *Nucl. Instrum. Meth. Phys. Res. B* **191** (2002) 810.
[124] R.I. Khaibullin, Yu.N. Osin, A.L. Stepanov and I.B. Khaibullin // Vacuum **51** (1998) 289.
[125] V.N. Popok, A.L. Stepanov and V.B. Odzhaev // *J. Appl. Spectr.* **72** (2005) 229.
[126] A.L. Stepanov and V.N. Popok // *Surf. Sci.* **566-568** (2004) 1250.
[127] V.N. Popok, A.G. Gromov, V.I. Nuzhdin, A.L. Stepanov // *J. Non-Cryst. Sol.* **356** (2010) 1258.
[128] C. Okay, B.Z. Rameev, R.I. Khaibullin, M. Okutan, F. Yildiz, V.N. Popok and B. Aktas // *Phys. Stat. Sol. (a)* **203** (2006) 1525.
[129] R. Nathawat, A. Kumar, V. Kulshrestha, Y.K. Vijay, T. Kobayashi and D. Kanjilal // *Nucl. Instrum. Meth Phys. Res. B* **266** (2008) 4749.
[130] S. Strbac, M. Nenadovic, Lj. Rajakovic and Z. Rakocevic // *Appl. Surf. Sci.* **256** (2010) 3895.
[131] M. Niklaus, S. Rosset, P. Dubois and H.R. Shea // *Mater. Res. Soc. Symp. Proc.* **1188** (2009) 1188-LL03-09.
[132] I.B. Khaibullin, R.I. Khaibullin, S.N. Abdullin, A.L. Stepanov, Yu.N. Osin, V.V. Bazarov and S.P. Kurzin // *Nucl. Instrum. Meth. Phys. Res. B* **127/128** (1997) 685.
[133] R.I. Khaibullin, Yu.N. Osin, A.L. Stepanov and I.B. Khaibullin // *Nucl. Instrum. Meth Phys. Res. B* **148** (1999) 1023.
[134] I.H. Loh, W.R. Oliver and P. Sioshansi // *Nucl. Instrum. Meth. Phys. Res. B* **34** (1988) 337.
[135] B. Wasserman // *Phys. Rev. B* **34** (1986) 1926.
[136] A. Moliton, B. Lucas, C. Moreau, R.H. Friend and B. Francois // *Philos. Mag. B* **69** (1994) 1155.
[137] J. Davenas and P. Thevenard // *Nucl. Instrum. Meth. Phys. Res. B* **80/81** (1993) 1021.
[138] T. Venkatesan, S.R. Forrest, M.L. Kaplan, C.A. Murray, P.H. Schmidt and B.J. Wilkens // *J. Appl. Phys.* **54** (1983) 3150.
[139] L.B. Bridwell, R.E. Giedd, Y.Q. Wang, S.S. Mohite, T. Jahnke, I.M. Brown, C.J. Bedell

and C.J. Sofield // *Nucl. Instrum. Meth. Phys. Res. B* **57** (1991) 656.
[140] F.F. Komarov, A.V. Leontyev and V.V. Grigoryev // *Nucl. Instrum. Meth. Phys. Res. B* **166-167** (2000) 650.
[141] C.J. Sofield, S. Sugden, J. Ing, L.B. Bridwell and Y.Q. Wang // Vacuum **44** (1993) 285.
[142] N.F. Mott and E.A. Devis, *Electronic Processes in Non-Crystalline Materials* (Clarendon, Oxford, 1979).
[143] Y. Wang, L.B. Bridwell and R.E. Giedd // *J. Appl. Phys.* **73** (1993) 474.
[144] V. Švorčik, V. Rybka, I. Miček, V. Popok, O. Jankovskij, V.Hnatowicz and J. Kvitek // *Eur. Polym. J.* **30** (1994) 1411.
[145] T. Chen, S. Yao, K. Wang, H. Wang and S. Zhou // *Surf. Coat. Technol.* **203** (2009) 3718.
[146] J. Bratko, B.O. Hall and K.F. Schoch, Jr. // *J. Appl. Phys.* **59** (1986) 1111.
[147] A.N. Aleshin, A.V. Gribanov, A.V. Dobrodumov, A.V. Suvorov and I.S. Shlimak // *Sov. Phys. Sol. State* **31** (1989) 6.
[148] O.Yu. Posudiyevskii, I.G. Myasnikova and A.A. Chuiko // *Dokl. Akad. Nauk SSSR* **319** (1991) 196, In Russian.
[149] W.M. Wang, H.H. Wan, T.W. Rong, J.R. Bao and S. H. Lin // *Nucl. Instrum. Meth. Phys. Res. B* **61** (1991) 466.
[150] G.B. Hadjichristov, V.K. Gueorguiev, Tz.E. Ivanova, Y.G. Marinov, V.G. Ivanov and E. Faulques // *Organic Electron.* **9** (2008) 1051.
[151] Y. Wu, T. Zhang, H. Zhang, X. Zhang, Zh. Deng and Gu Zhou // *Nucl. Instrum. Meth. Phys. Res. B* **169** (2000) 89.
[152] M. Niklaus and H.R. Shea // *Acta Mater.* **59** (2011) 830.
[153] P.A. Lee and T.V. Ramakrishnan // *Rev. Mod. Phys.* **57** (1985) 287.
[154] A.G. Zabrodskii and K.N. Zinov'ev // *J. Experim. Theoret. Phys.* **59** (1984) 425.
[155] S. Vionnet-Menot, C. Grimaldi, T. Maeder, S. Strässler and P. Ryser // *Phys. Rev. B* **71** (2005) 064201.
[156] T. Hioki, S. Noda, M. Sigmund, M. Kakeno, K. Yamada and J. Kawamoto // *Appl. Phys. Lett.* **43** (1983) 30.
[157] J. Robertson // *Adv. Phys.* **35** (1986) 317.
[158] J. Tauc, R. Grigorovici and A. Vancu // *Phys. Stat. Sol.* **15** (1966) 627.
[159] L. Calcagno and G. Foti // *Nucl. Instrum. Meth. Phys. Res. B* **59/60** (1991) 1153.
[160] A. Kondyurin, R. Khaibullin, N. Gavrilov and V. Popok // Vacuum **68** (2002) 341.
[161] E. Yap, D.G. McCulloch, D.R. McKenzie, M.V. Swain, L.S. Wielunski and R.A. Clissold // *J. Appl. Phys.* **83** (1998) 3404.
[162] J. Davenas and P. Thevenard // *Nucl. Instrum. Meth. Phys. Res. B* **59/60** (1991) 1249.
[163] D.M. Rück, J. Schulz and N. Deusch // *Nucl. Instrum. Meth. Phys. Res. B* **131** (1997) 149.
[164] G.B. Hadjichristov, V. Ivanov and E. Faulques // *Appl. Surf. Sci.* **254** (2008) 4820.
[165] T. Tsvetkova, S. Balabanov, L. Avramov, E. Borisova, I. Angelov, S. Sinning and L. Bischoff // *Vacuum* **83** (2009) S252.
[166] C. Flytzanis, F. Hache, M.C. Klein, D. Ricard, P. Rousignol, *Nonlinear optics in composite materials* (Elsevier, Amsterdam, 1991).
[167] A.L. Stepanov, R.I. Khaibullin and I.B. Khaibullin // *Phil. Mag. Lett.* **77** (1998) 261.
[168] W. Yuguang, Z. Tonghe, L. Andong and Z. Gu // *Surf. Coat. Technol.* **157** (2002) 262.
[169] A.L. Stepanov, V.N. Popok, I.B. Khaibullin and U. Kreibig // *Nucl. Instrum. Meth. Phys. Res. B* **191** (2002) 473.
[170] A.L. Stepanov, S.N. Abdullin, V.Yu. Petukhov, Yu.N. Osin, R.I. Khaibullin and I.B. Khaibullin // *Phil. Mag. B* **80** (2000) 23.
[171] H. Boldyryeva, N. Kishimoto, N. Umeda, K. Kondo, O.A. Plaksin and Y. Takeda // *Nucl. Instrum. Meth Phys. Res. B* **219-220** (2004) 953.
[172] N. Umeda, V.V. Bandourko, V.N. Vasilets, N. Kishimoto // *Nucl. Instrum. Meth Phys. Res. B* **206** (2003) 657.
[173] M. Quinten, *Optical properties of nanoparticle systems* (Wiley-VCH, Weinheim, 2011).
[174] Z.J. Han and B.K. Tay // *Nucl. Instrum. Meth Phys. Res. B* **267** (2009) 496.
[175] M.A. Magrupov // *Uspekhi Khimii* **50** (1981) 2106, in Russian.
[176] I.B. Goldberg, H.R. Crove, P.R. Newman, A.J. Heeger and A.G. MacDiarmid // *Chem. Phys.* **70** (1979) 1132.
[177] T.S. Zhuravleva // *Uspekhi Khimii* **LVI** (1987) 128, in Russian.
[178] V.A. Polyboyarov, O.V. Andryushkova, M.Yu. Bulynnikova // *Sib. Khim. Zhurn.* **5** (1992) 128, in Russian.

[179] K. Ogawa, *U.S. Patent* No. 4,751.100 (1988).
[180] A.L. Stepanov, R.I. Khaibullin, S.N. Abdullin, Yu.N. Osin, V.F. Valeev and I.B. Khaibullin // *Inst. Phys. Conf. Ser. Proc.* **147** (1995) 357.
[181] B.Z. Rameev, B. Aktas, R.I. Khaibullin, V.A. Zhikharev, Yu.N. Osin and I.B. Khaibullin // Vacuum **58** (2000) 551.
[182] J.C. Pivin, R. Khaibullin, B.Z. Rameev and M. Dubus // *J. Non-Cryst. Sol.* **333** (2004) 48.
[183] R. Malik, R. Sharma, D. Kanjilal and S. Annapoorni // *J. Phys. D: Appl. Phys.* **42** (2009) 235501.
[184] Ch. Kittel, *Introduction to Solid State Physics*, 3d ed. (Willey, New York, 1968), p.525.
[185] G.V. Skrotskii, L.V. Kurbatov, In: *Ferromagnetic Resonance*, ed. by S.V. Vonsovskii (Pergamon: Oxford, 1966), p. 345.
[186] M.G. Lukashevich, X. Battle, A. Labarta, V.N. Popok, V.A. Zhikharev, R.I. Khaibullin and V.B. Odzhaev // *Nucl. Instrum. Meth. Phys. Res. B* **257** (2007) 589.
[187] Yu.G. Pogorelov, G.N. Kakazei, M.M.P. de Azevedo and J.B. Sousa // *J. Magnet. Magn. Mater.* **196-197** (1999) 112.
[188] V.N. Popok, M.G. Lukashevich, N.I. Gorbachuk, V.B. Odzhaev, R.I. Khaibullin and I.B. Khaibullin // *Phys. Stat. Sol. (a)* **203** (2006) 1545.
[189] C. Tian-Xiang, Y. Shu-De, H. Wei, F. Tao, L. Lin, Z. Sheng-Qiang // Chin. Phys. Lett. **26** (2009) 087201.
[190] Y.Q. Wang, D. Robey, R.E. Giedd and M.G. Moss // *Mater. Res. Soc. Symp. Proc.* **316** (1994) 349.
[191] C. De Julian Fernandez, M.G. Manera, J. Spadavecchia et al. // *Sensors Actuat. B* **111-112** (2005) 225.
[192] M. Guenther, G. Gerlach, G. Suchaneck, K. Sahre, K.-J. Eichhorn, V. Baturin and S. Duvanov // *Nucl. Instrum. Meth. Phys. Res. B* **216** (2004) 143.